Advances in Water Resources 153 (2021) 103951

Contents lists available at ScienceDirect

Advances in Water Resources

journal homepage: www.elsevier.com/locate/advwatres

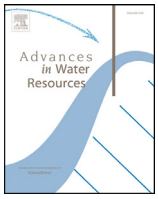

Conservative numerical methods for the reinterpreted discrete fracture model on non-conforming meshes and their applications in contaminant transportation in fractured porous media

Hui Guo [a,1], Wenjing Feng [b], Ziyao Xu [c], Yang Yang [d,2,*]

[a] College of Science, China University of Petroleum, Qingdao 266580, China
[b] College of Science, China University of Petroleum, Qingdao 266580, China
[c] Division of Applied Mathematics, Brown University, Providence, RI 02912 United States
[d] Department of Mathematical Sciences, Michigan Technological University, Houghton, MI 49931 United States

ARTICLE INFO

Keywords:
Reinterpreted discrete fracture model
Non-conforming meshes
Incompressible miscible displacements
Interior penalty discontinuous Galerkin method
Enriched Galerkin method
Bound-preserving

ABSTRACT

The discrete fracture model (DFM) has been widely used to simulate fluid flow in fractured porous media. Traditional DFM is considered to be limited on conforming meshes, hence significant difficulty may arise in generating high-quality unstructured meshes due to the complexity of the fracture networks. Recently, Xu and Yang reinterpreted DFM and demonstrated that it can actually be extended to non-conforming meshes without any essential changes. However, the continuous Galerkin (CG) method was applied and the local mass conservation was missing. This paper is a follow-up work, and we apply the interior penalty discontinuous Galerkin (IPDG) method and enriched Galerkin (EG) method for the pressure equation. With the numerical fluxes, the local mass is conservative. As an application, we combine the reinterpreted DFM (RDFM) with the incompressible miscible displacements in porous media. The bound-preserving techniques are applied to the coupled system. We can theoretically guarantee that the concentration is between 0 and 1. Finally, several numerical experiments are given to demonstrate the good performance of the RDFM based on the above two methods on non-conforming meshes and the effectiveness of the bound-preserving technique.

1. Introduction

Numerical simulation of fluid flow in fractured porous media is of great significance for improving oil recovery in naturally fractured reservoirs, contaminant transport in fractured rocks and underground radioactive waste reservoirs. Due to the high conductivity and complexity of the fracture networks, it is critical but still challenging to accurately establish the effect of fractures on the flow in fractured media.

In recent decades, as one of the most important models of the flow simulation in fractured porous media, the discrete fracture model (DFM) has been intensively analyzed. In 1982, Noorishad and Mehran (1982) introduced the first DFM for a single-phase flow. Subsequently, Baca et al. (1984) studied DFM for the heat and solute transport in fractured media on conforming meshes. The basic idea was to treat the flow in one-dimensional fractures and two-dimensional matrix respectively by using the hybrid-dimensional method, and then coupled them with the fracture system multiplied by the fracture thickness as a dimensional homogeneity factor according to the principle of superposition. Later, Kim and Deo (1999, 2000), Karimi-Fard and Firoozabadi (2001) used the Galerkin finite element methods to solve the multiphase flow combined with DFM. In addition, finite volume methods were also explored, e.g. Box-DFM (Monteagudo and Firoozabadi, 2004; Reichenberger et al., 2006; Monteagudo and Firoozabadi, 2007b; 2007a; Zhang et al., 2016) and the cell-centered finite volume DFM (CC-DFM) (Karimi-Fard et al., 2003; Sandve et al., 2012; Ahmed et al., 2015; Gläser et al., 2017; Fang et al., 2018). Moreover, Hoteit and Firoozabadi (2005, 2006, 2008), Moortgat and Firoozabadi (2013a,b), Zidane and Firoozabadi (2014) and Moortgat et al. (2016) obtained the local mass conservation and high accuracy of the flow and transport equations in fractured media by combining the mixed finite element (MFE) and the discontinuous Galerkin (DG) methods in DFM. For other methods of DFM, we can refer to Xu and Yang (2020) and the references therein.

* Corresponding author.
E-mail address: yyang7@mtu.edu (Y. Yang).

[1] Supported by the Fundamental Research Funds for the Central Universities 20CX05011A and the Major Scientific and Technological Projects of CNPC under Grant ZD2019-183-008.
[2] Supported by NSF grant DMS-1818467.

https://doi.org/10.1016/j.advwatres.2021.103951
Received 18 January 2021; Received in revised form 20 April 2021; Accepted 16 May 2021
Available online 20 May 2021

Unfortunately, the above methods can only be applied to conforming meshes, i.e. fractures must be located at the edges of the triangular/retangular elements. It is very difficult to generate high quality meshes, especially when the fracture network is complex and the distances or angles among fractures are small. To overcome this shortcoming, the embedded discrete fracture model (EDFM) (Li and Lee, 2008; Moinfar, 2013; Yan et al., 2016; Ţene et al., 2017; Jiang and Younis, 2017; HosseiniMehr et al., 2018; Xu et al., 2019) was proposed as an alternative. In the EDFM, all fractures are discretized into segments by the background matrix mesh, forming the so-called fracture cells in contrast with the matrix cells, and the cells of both types are assigned with separate degrees of freedom (DoF). The key idea of EDFM is to define the non-neighboring connections (NNCs) between different cells, i.e. the connections between a fracture cell and the matrix cell it penetrates, connected fracture cells in neighboring matrix cells and intersecting fracture cells in the same matrix cell. Then we can compute the mass transfer in each NNC pair. For instance, the mass transfer between the fracture-matrix NNC pair is determined by the average normal distance between the fracture cell and the matrix cell. The mass transfer between other NNC pairs is evaluated accordingly, see Moinfar (2013) for more details. Though eliminates the constraint of conforming meshes, the EDFM requires a large amount of computation on the transmissibility factors of NNCs in the pre-processing and the special treatment when several fractures intersect at the same point. The number of NNCs and DoF increase rapidly as the fracture networks are getting more and more complicated. In addition, many other methods were proposed, such as the non-conforming finite element method (Köppel et al., 2019a; 2019b; Schädle et al., 2019) based on Lagrange multipliers, the extended finite element discrete fracture model (XFEM-DFM) (Fumagalli and Scotti, 2014)-ter et al. (2019),Martin et al. (2005), Salimzadeh and Khalili (2015), Angot et al. (2009), Angot (2003), Huang et al. (2011), Alboin et al. (2000), Flemisch et al. (2016), Hansbo and Hansbo (2002) and the CutFEM (Burman et al., 2019). However, these methods have some disadvantages, such as high computational cost or not suitable for complex fracture networks.

Recently, Xu and Yang (2020) reinterpreted the DFM and proposed the mathematical expression in 2020. The reinterpreted DFM (RDFM) illustrates that the traditional DFM (Kim and Deo, 1999; 2000; Karimi-Fard and Firoozabadi, 2001) is actually not limited on conforming meshes. The authors proposed a hybrid-dimensional representation of the permeability tensor, describing the fracture as a one-dimensional line Dirac-δ functions contained in the permeability tensor. By using the traditional continuous Galerkin (CG) finite element methods, the RDFM for single phase flow on non-conforming meshes was derived. Numerical experiments showed the advantages of the RDFM. However, the local mass conservation is missing. To fix this gap, we construct the numerical fluxes in the scheme, and would like to apply the DG methods.

DG methods employ finite element spaces containing elementwise discontinuous functions and develop special numerical techniques to control the jumps of numerical approximations as well as the nonlinearity of the convection term. A commonly used DG method for convection-diffusion equations and elliptic equations is the interior penalty DG (IPDG) method (Rivière, 2008). The IPDG method in this paper is a symmetric form, i.e. symmetric interior penalty Galerkin (SIPG) (Sun and Wheeler, 2005b). In Antonietti et al. (2019), P. Antonietti et al proposed a DG approximation of flows in fractured porous media on polytopic grids. Though the DG methods can preserve local mass conservation, compared to the CG methods, there are more DoF. In view of this situation, Becker et al. (2003) first proposed the enriched Galerkin (EG) finite element method for solving the time-independent convection-diffusion and Stokes problems. The basic idea is to enrich the continuous Galerkin finite element space with elementwise constant functions. Later, Sun and Liu (2009) applied high-order EG methods to the coupled system of flow and transport equations and constructed conservative fluxes. EG and DG methods are both locally mass conservative, but the DoF of EG method is slightly larger than that of CG method and much less than that of DG method. Recently, the EG method has been developed to solve general elliptic and parabolic problems with dynamic mesh adaptivity (Lee and Wheeler, 2017; Lee et al., 2018) and jump condition (Rupp and Lee, 2020; Lee et al., 2016a), and extended to multiphase fluid flow problems (Lee and Wheeler, 2020; 2018; Kadeethum et al., 2020b), poroelastic problems (Choo and Lee, 2018; Kadeethum et al., 2020a; 2021), phase-field fracture problems (Wheeler et al., 2020; Lee et al., 2016b; 2018), shallow water equations (Hauck et al., 2020). In Lee and Wheeler (2020), Lee and Wheeler used EG method to simulate two-phase flow in propagating fractures with relative permeability and capillary pressure. Subsequently, Kadeethum et al. (2020b) employed EG method for fluid flow in porous media with low dimensional fractures. Moreover, Rupp and Lee (2020) constructed a novel EG finite element method by enriching the CG space with not only piecewise constants but also piecewise polynomials with an arbitrary order.

As an application, we apply the RDFM given in Xu and Yang (2020) to contaminant transportation and study the miscible displacements in porous media. In Douglas et al. (1983b,a), Douglas et al. first proposed the mixed finite element method for incompressible miscible displacements. The compressible problems were also developed in Douglas and Roberts (1983) and Chou and Li (1991). In recent years, the DG methods have been widely used for solving the compressible miscible displacements (Cui, 2008; Yang, 2011; Guo and Zhang, 2015; Guo et al., 2017) and incompressible miscible displacements (Bartels et al., 2009; Guo et al., 2014; Yu et al., 2017; Kumar, 2012; Sun et al., 2002; Sun and Wheeler, 2005a) in porous media. As another important aspect of DG methods, the bound-preserving technique has been widely studied, which can obtain physically relevant approximations. In Zhang and Shu (2010), Zhang and Shu first constructed the genuinely maximum-principle-satisfying high order DG and finite volume methods. If the exact solution has only one lower bound 0, then the technique is also called positivity-preserving technique. However, few papers focused on bound-preserving techniques for the miscible displacements. In many actual problems, physical parameters are closely related to the concentration c. If c is out of the interval 0 to 1, we might not obtain the parameters used in the system, and the numerical approximations may blow up in some extreme cases (Guo and Yang, 2017). In Guo and Yang (2017), Guo and Yang proposed the first bound-preserving DG methods for the coupled system of the two-component compressible miscible displacements. The basic idea is as follows (1) Use the pressure equation to subtract the concentration equation to obtain the concentration of the second component. (2) Apply the positivity-preserving techniques to both c_1 and c_2 (c_i is the concentration of the ith component of the flow), respectively. (3) Enforce $c_1 + c_2 = 1$ by choosing consistent numerical fluxes (see Definition 2.1) in the pressure and concentration equations. In Guo and Yang (2017), the authors theoretically proved that the above algorithm can yield physically relevant numerical cell averages. Then a slope limiter can be applied to make the numerical approximations to be within the desired bounds. Later, in Chuenjarern et al. (2019), Chuenjarern et al. extended the idea to multi-component miscible displacements and proposed high-order bound-preserving DG methods on triangular mesh, and proved that the limiter does not affect the accuracy. The bound-preserving finite difference methods were also discussed in Guo et al. (2020).

In this paper, we first apply the RDFM in Xu and Yang (2020) to the incompressible miscible displacements in fractured porous media. There are two main contributions. (1) We derive the EG scheme and IPDG scheme for the flow equation and the IPDG scheme for the transport equation, and construct conservative fluxes, leading to local mass conservation. (2) We theoretically construct the bound-preserving technique by using the EG method and IPDG method for solving the pressure and concentration equations, respectively. We state that this paper is very different from the previous works. Firstly, different from Xu and Yang (2020), the numerical methods in this paper are locally conservative by design, while the CG method in Xu and Yang (2020) is not. Moreover, due to the discontinuity nature of the numerical method, the

contribution of the Dirac δ-function in the numerical fluxes has to be treated effectively. In fact, we substitute the expressions of the normal component of velocity into the scheme of concentration, and calculate the integral of the δ-function exactly to obtain the numerical fluxes at the cell interfaces intersecting with fractures. Secondly, different from Guo and Yang (2017) and Chuenjarern et al. (2019), where DG methods were used to solve both the pressure and concentration equations, the bound-preserving technique studied in this paper combines the EG and IPDG method. In Guo and Yang (2017) and Chuenjarern et al. (2019), we subtract the scheme of the concentration equation form that of the pressure equation to obtain that of the second concentration by using consistent flux pairs. However, in this paper, it is impossible to obtain the numerical scheme for the second concentration by subtracting schemes for the pressure and concentration equations due to the mismatch of the finite element spaces. Though the discrete spaces of the two methods are different, we only need to analyze the cell averages. In fact, with the physically relevant numerical cell averages, the bounds of the numerical approximations can be preserved by applying suitable slope limiters. To preserve the bounds of the numerical cell averages, we only need the consistent flux pairs (see the Definition 2.1) and the positivity-preserving technique. Finally, we claim that all the algorithms demonstrated in this paper can be extended to compressible flows with some minor changes following Guo and Yang (2017) and Chuenjarern et al. (2019). In addition to the above, the computational cost in our pre-processing is much less since we only need to compute the intersection between fractures and cell interfaces rather than the average normal distance between fracture cells and matrix cells, and it is not necessary to consider flux interchange between intersecting fractures. Moreover, the DoF in our method keeps the same as the number of fractures increases. For more information about the computational cost, we can refer to Xu and Yang (2020).

The paper is organized as follows. In Section 2, we introduce the model of incompressible miscible displacements in fractured porous media, and derive the EG scheme and IPDG scheme for the flow equation as well as the IPDG scheme for the transport equation. In Section 3, we discuss the bound-preserving techniques. Numerical experiments are given in Section 4. Finally, we end in Section 5 with concluding remarks.

2. Governing equations and numerical schemes

2.1. Governing equations

In this paper, we consider the incompressible miscible displacements in fractured porous media. Let $\Omega = [0,1]\times[0,1]$ be a bounded rectangular domain in $\mathbb{R}^2$. We consider the fluid mixture with two components, and the flow Eq. (2.1) and transport Eq. (2.2) have the following forms:

$$-\nabla\cdot(\mathbf{K}\nabla p) \equiv \nabla\cdot\mathbf{u} = q, \quad (x,y)\in\Omega,\ 0<t\le T, \tag{2.1}$$

$$\phi c_t + \nabla\cdot(\mathbf{u}c) - \nabla\cdot(\mathbf{D}(\mathbf{u})\nabla c) = \tilde{c}q, \quad (x,y)\in\Omega,\ 0<t\le T, \tag{2.2}$$

where the unknown variables p, $\mathbf{u}$ and c are the pressure of the fluid mixture, the Darcy velocity of the mixture, and the volumetric concentration of interested species, respectively. ϕ is the porosity of the rock. q is the external volumetric flow rate, $\tilde{c}$ is the concentration of the fluid in the external flow. $\tilde{c}$ must be specified at points where injection ($q>0$) takes place, and is assumed to be equal to c at production points ($q<0$). The diffusion coefficient $\mathbf{D}$ is symmetric and arises from two aspects: molecular diffusion, which is rather small for field-scale problems, and dispersion, which is velocity-dependent. It takes the form

$$\mathbf{D}(\mathbf{u}) = \phi(x,y)(d_{mol}\mathbf{I} + d_{long}|\mathbf{u}|\mathbf{E} + d_{tran}|\mathbf{u}|\mathbf{E}^{\perp}), \tag{2.3}$$

where $\mathbf{E}$, a 2×2 matrix, represents the orthogonal projection along the velocity vector and is given by

$$(\mathbf{E}(\mathbf{u}))_{ij} = \frac{u_i u_j}{|\mathbf{u}|^2}, \quad 1\le i,j\le 2,\ \mathbf{u}=(u_1,u_2),$$

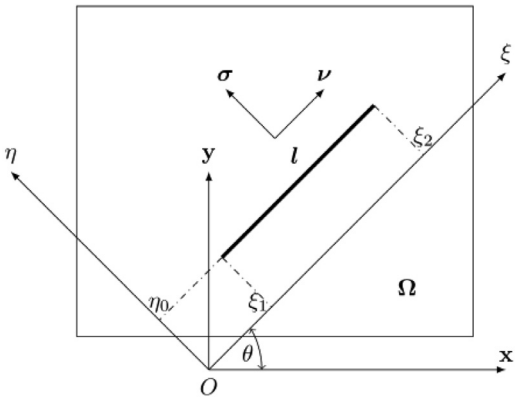

Fig. 1. Fractured media and the corresponding coordinate systems.

and $\mathbf{E}^{\perp} = \mathbf{I} - \mathbf{E}$ is the orthogonal complement. The diffusion coefficient d_{long} measures the dispersion in the direction of the flow and d_{tran} shows that transverse to the flow. To ensure the stability of the scheme, in almost all of the previous works, $\mathbf{D}$ is assumed to be strictly positive definite. In this paper, we assume $\mathbf{D}$ to be positive semidefinite. Therefore, we have $D_{11}\ge 0$, $D_{22}\ge 0$, and $D_{12}=D_{21}$. Moreover, the pressure is uniquely determined up to a constant, thus we assume $\int_\Omega p\,dx\,dy = 0$ to ensure the uniqueness. However, this assumption is not essential. In this paper, we consider a two component displacement only and the relationship of components can be stated as follows:

$$c = c_1 = 1 - c_2,$$

where c_i is the concentration of the ith component of the fluid mixture. $\mathbf{K}$ is the permeability tensor. Following Xu and Yang (2020), for fractured porous media, $\mathbf{K}$ can be expressed as follows

$$\mathbf{K} = \mathbf{K}_m + \epsilon k_f \delta(\eta-\eta_0)\mathbf{1}(\xi_1\le\xi\le\xi_2)\boldsymbol{\nu}\boldsymbol{\nu}^T, \tag{2.4}$$

where $\mathbf{K}_m$, ϵ, and k_f are the permeability tensor of matrix, the thickness of the fracture, and the tangential permeability of the fracture, respectively. $\mathbf{1}(\cdot)$ is the indicator function defined as $\mathbf{1}(\text{expr})$ equals 1 if expr is true while equals 0 otherwise. $\boldsymbol{\nu}$ is the tangential unit vector of the fracture. For variable η and ξ, see Fig. 1. $\xi o\eta$ and xoy are local coordinate system associated with the fracture l and global coordinate system, respectively. We notice that $\delta(\eta-\eta_0)\mathbf{1}(\xi_1\le\xi\le\xi_2)$ contains the information of position of the fracture.

For any point $m\in\Omega$, the transformation between its local coordinates (ξ_m,η_m) and global coordinates (x_m,y_m) is given as

$$\begin{bmatrix}\xi_m\\ \eta_m\end{bmatrix} = \begin{bmatrix}\cos(\theta) & \sin(\theta)\\ -\sin(\theta) & \cos(\theta)\end{bmatrix}\begin{bmatrix}x_m\\ y_m\end{bmatrix},$$

where θ is the angle of the fracture. By the coordinates transformation, the expression of $\mathbf{K}$ under global coordinates xoy is

$$\mathbf{K} = \mathbf{K}_m + \epsilon k_f \delta(-\sin(\theta)x+\cos(\theta)y-\eta_0)\mathbf{1}(\xi_1\le\cos(\theta)x+\sin(\theta)y\le\xi_2)\boldsymbol{\nu}\boldsymbol{\nu}^T. \tag{2.5}$$

Following Xu and Yang (2020), we call the expression $\mathbf{K}$ in (2.5) the hybrid-dimensional representation of permeability tensor, because the matrix part $\mathbf{K}_m$ in (2.5) is of rank 2 and has a 2D support while the fracture part $\epsilon k_f\delta(\cdot)\mathbf{1}(\cdot)\boldsymbol{\nu}\boldsymbol{\nu}^T$ is of rank 1 and has a 1D support. The expression above is only for fractured media with single fracture but can be extended to a fracture network as

$$\mathbf{K} = \mathbf{K}_m + \sum_{i=1}^{L}\epsilon_i k_{fi}\delta_i(\cdot)\mathbf{1}_i(\cdot)\boldsymbol{\nu}_i\boldsymbol{\nu}_i^T, \tag{2.6}$$

where L is the number of fractures, $\delta_i(\cdot)$ and $\mathbf{1}_i(\cdot)$ are the shorthands of their full expressions in (2.4) and (2.5), ϵ_i, k_{fi} and $\boldsymbol{\nu}_i$ are the thickness, the tangential permeability, and the tangential unit vector of the ith

fracture, respectively. See Xu and Yang (2020) for more information about $\mathbf{K}$, which is an important reinterpretation and extension of DFM.

In this paper, we consider the mixed boundary condition for the flow equation:

$$p = p_D, \quad \mathbf{x} \in \Gamma_D \subset \partial\Omega; \quad \mathbf{u}\cdot\mathbf{n} \equiv -\mathbf{K}\nabla p\cdot\mathbf{n} = p_N, \quad \mathbf{x} \in \Gamma_N := \partial\Omega\backslash\Gamma_D. \tag{2.7}$$

For the transport equation, we consider the following boundary conditions:

$$(\mathbf{u}c - \mathbf{D}(\mathbf{u})\nabla c)\cdot\mathbf{n} = c_{in}\mathbf{u}\cdot\mathbf{n}, \quad \mathbf{x} \in \Gamma_{in}, \tag{2.8}$$

$$\mathbf{D}(\mathbf{u})\nabla c\cdot\mathbf{n} = 0, \quad \mathbf{x} \in \partial\Omega\backslash\Gamma_{in}, \tag{2.9}$$

where $\mathbf{n}$ is the unit outer normal vector of the boundary $\partial\Omega$; $\Gamma_{in} := \{x \in \Gamma_D : \mathbf{u}\cdot\mathbf{n} < 0\}$ is the inflow boundary. For convenience, we assume $P_N = 0$, and$\Gamma_D = \overline{\Gamma}_{in} \cup \overline{\Gamma}_{out}$ in this paper, where $\Gamma_{out} := \{x \in \Gamma_D : \mathbf{u}\cdot\mathbf{n} > 0\}$ is the outflow boundary. In fact, if $p_N < 0$, Γ_N is also a member of the inflow boundary; if $p_N > 0$, Γ_N is the outflow boundary. Therefore, this assumption is not essential.

Moreover, the initial concentration is given as

$$c(x, y, 0) = c_0(x, y), \quad (x, y) \in \Omega. \tag{2.10}$$

2.2. Basic notations

We demonstrate the notations to be used throughout the paper. We consider rectangular meshes only, the techniques for triangular meshes can be obtained following the same lines given in Sun and Liu (2009) and Chuenjarern et al. (2019) with some minor changes. Let $0 = x_{\frac{1}{2}} < \cdots < x_{N_x+\frac{1}{2}} = 1$ and $0 = y_{\frac{1}{2}} < \cdots < y_{N_y+\frac{1}{2}} = 1$ be the grid points in the x and y directions, respectively. Define $I_i = (x_{i-\frac{1}{2}}, x_{i+\frac{1}{2}})$ and $J_j = (y_{j-\frac{1}{2}}, y_{j+\frac{1}{2}})$. Let $K_{ij} = I_i \times J_j$ be a partition of Ω and denote $\Omega_h = \cup_{i,j} K_{ij}$. For simplicity, we use K to denote a typical cell. We use Γ for all the cell interfaces, and $\Gamma_0 = \Gamma\backslash\partial\Omega$ is the set of interior edges. For any $e \in \Gamma$, denote $|e|$ to be the length of e. Moreover, we define $\mathbf{n}_e = \mathbf{n}_x = (1, 0)$ if e is parallel to the y-axis while $\mathbf{n}_e = \mathbf{n}_y = (0, 1)$ if e is parallel to the x-axis. Furthermore, we denote $\partial\Omega_+ = \{e \in \partial\Omega : \mathbf{n} = \mathbf{n}_e\}$, where $\mathbf{n}$ is the unit outer normal of $\partial\Omega$, and $\partial\Omega_- = \partial\Omega\backslash\partial\Omega_+$. The mesh size in the x and y directions are given $\Delta x_i = x_{i+\frac{1}{2}} - x_{i-\frac{1}{2}}$ and $\Delta y_j = y_{j+\frac{1}{2}} - y_{j-\frac{1}{2}}$, respectively. For simplicity, we assume uniform meshes and denote $\Delta x = \Delta x_i$ and $\Delta y = \Delta y_j$. However, this assumption is not essential. The finite element space is chosen as

$$W_h^k = \{z : z|_K \in Q^k(K),\ \forall K \in \Omega_h\},$$

where $Q^k(K)$ denotes the space of tensor product polynomials of degrees at most k in K. We choose $\boldsymbol{\beta} = (1, 1)^T$ to be a fixed vector that is not parallel to any normal of the element interfaces. As we know, $\forall e \in \Gamma_0$ is shared by two elements K_ℓ and K_r, where $\boldsymbol{\beta}\cdot\mathbf{n}_\ell > 0$, and $\boldsymbol{\beta}\cdot\mathbf{n}_r < 0$, with $\mathbf{n}_\ell$ and $\mathbf{n}_r$ being the outward normals of K_ℓ and K_r. For any $z \in W_h^k$, z^- and z^+ represent the values taken from K_ℓ and K_r, respectively. Furthermore, we use $[z] = z^+ - z^-$ and $\{z\} = \frac{1}{2}(z^+ + z^-)$ as the jump and average of z at the cell interfaces, respectively.

2.3. EG and IPDG methods for the flow equation

In this subsection, we use EG and IPDG methods for the flow equation, both preserves the local mass conservation. Furthermore, the EG method combines the advantages of both CG and DG methods. This method preserves the local mass conservation of DG method, while the degree of freedom is close to that of CG method. Moreover, the EG method has a similar weak formulation as for the DG method, yet whose implementation is simpler and more efficient.

Now we first define the space of continuous piecewise polynomials

$$W_h^{k,C} = W_h^k \cap C(\Omega),$$

where $C(\Omega)$ represents the set of continuous functions in Ω. Then we define

$$W_h^{k,C_0} = W_h^{k,C} \cup W_h^0,$$

which is called EG space by enriching the CG approximation space with piecewise constant functions.

For simplicity, if not otherwise stated, we use p, $\mathbf{u}$, c as the numerical approximations from now on, then the EG scheme for (2.1) is to find $p \in W_h^{k,C_0}$ such that for any $\xi \in W_h^{k,C_0}$, we have

$$a_0(p, \xi) + a_D(p, \xi) = F(\xi), \tag{2.11}$$

where

$$\begin{aligned} a_0(p, \xi) = (\mathbf{K}\nabla p, \nabla\xi) &+ \sum_{e\in\Gamma_0}\int_e \{\mathbf{K}\nabla p\cdot\mathbf{n}_e\}[\xi]ds + \sum_{e\in\Gamma_0}\frac{\sigma_e}{|e|^\beta}\int_e [p][\xi]ds \\ &+ \sum_{e\in\Gamma_0}\frac{\alpha_e}{|e|^\gamma}\int_e \delta(\cdot)\mathbf{1}(\cdot)[p][\xi]|\boldsymbol{\nu}\cdot\mathbf{n}_e|ds + \sum_{e\in\Gamma_0}\int_e \{\mathbf{K}\nabla\xi\cdot\mathbf{n}_e\}[p]ds, \end{aligned} \tag{2.12}$$

$$\begin{aligned} a_D(p, \xi) = &-\sum_{e\in\Gamma_D}\int_e \mathbf{K}\nabla p\cdot\mathbf{n}_{e,D}\xi ds + \sum_{e\in\Gamma_D}\frac{\sigma_e}{|e|^\beta}\int_e p\xi ds \\ &-\sum_{e\in\Gamma_D}\int_e \mathbf{K}\nabla\xi\cdot\mathbf{n}_{e,D}p ds, \end{aligned} \tag{2.13}$$

$$\begin{aligned} F(\xi) = (q, \xi) &- \sum_{e\in\Gamma_N}\int_e p_N\xi ds + \sum_{e\in\Gamma_D}\frac{\sigma_e}{|e|^\beta}\int_e p_D\xi ds \\ &- \sum_{e\in\Gamma_D}\int_e \mathbf{K}\nabla\xi\cdot\mathbf{n}_{e,D}p_D ds. \end{aligned} \tag{2.14}$$

Here Γ_0 represents the set of interior edges. Γ_D and Γ_N represent the sets of Dirichlet and Neumann boundaries, respectively. σ_e and α_e are two positive constants on each edges e. $\mathbf{n}_{e,D}$ is the unit outer normal vector of $e \in \Gamma_D$. β and γ are two positive constants, usually greater than or equal to 1. $(u, v) = \sum_{K\in\Omega_h}\int_K uvdxdy$, $\int_e gds$ is a line integral with respect to g for $2D$ case.

Using the hybrid-dimensional representation of $\mathbf{K}$ established in (2.5), we have

$$\mathbf{K}\nabla p\cdot\nabla\xi = \mathbf{K}_m\nabla p\cdot\nabla\xi + \epsilon k_f\delta(\cdot)\mathbf{1}(\cdot)\frac{\partial p}{\partial\boldsymbol{\nu}}\frac{\partial\xi}{\partial\boldsymbol{\nu}}, \tag{2.15}$$

$$\mathbf{K}\nabla p\cdot\mathbf{n}_e = \mathbf{K}_m\nabla p\cdot\mathbf{n}_e + \epsilon k_f\delta(\cdot)\mathbf{1}(\cdot)\frac{\partial p}{\partial\boldsymbol{\nu}}\boldsymbol{\nu}\cdot\mathbf{n}_e. \tag{2.16}$$

Following Lemma 4.1 in Xu and Yang (2020),

$$\int_\Omega \delta(\cdot)\mathbf{1}(\cdot)g(x, y)dxdy = \int_l g(x, y)ds, \tag{2.17}$$

where the line segment l is the support of $\delta(\cdot)\mathbf{1}(\cdot)$ as shown in Fig. 1. Notice that there is no fracture intersects the boundary, so $\mathbf{K} = \mathbf{K}_m$ on $\partial\Omega$.

For $\sum_{e\in\Gamma_0}\int_e \delta(\cdot)\mathbf{1}(\cdot)g(x, y)ds$, we have the following lemma, whose proof will be given in Appendix A.

Lemma 2.1. *Let $\delta(\cdot)$ and $\mathbf{1}(\cdot)$ be the shorthands of their full expression in (2.4) and (2.5). For any continuous function g on Ω, we have*

$$\int_e \delta(\cdot)\mathbf{1}(\cdot)g(x, y)ds = g(x^*, y^*)\cdot\frac{1}{|\boldsymbol{\nu}\cdot\mathbf{n}_*|}, \tag{2.18}$$

where (x^*, y^*) is the coordinate of intersection point between the fracture l and curve e, $\boldsymbol{\nu}$ is the unit tangential vector of fracture l, and $\mathbf{n}_*$ is the unit normal vector of curve e at (x^*, y^*).

With the lemma, we can get $\sum_{e\in\Gamma_0}\int_e \delta(\cdot)\mathbf{1}(\cdot)g(x,y)ds = \sum_{(x^*,y^*)\in X_f} g(x^*,y^*)\cdot\frac{1}{|\boldsymbol{\nu}\cdot\mathbf{n}_*|}$ immediately, where X_f represents the set of intersection points between the fracture and all the cell interior interfaces, and $\mathbf{n}_*$ is the unit normal vector of edge e at (x^*,y^*).

Based on (2.15)–(2.18), we can obtain the final version of the EG scheme for (2.1) in fractured porous media: find $p\in W_h^{k,C_0}$ such that for any $\xi\in W_h^{k,C_0}$,

$$\tilde{a}_0(p,\xi)+a_D(p,\xi)+a_l(p,\xi)=F(\xi), \tag{2.19}$$

where

$$\tilde{a}_0(p,\xi)=(\mathbf{K}_m\nabla p,\nabla\xi)+\sum_{e\in\Gamma_0}\int_e\{\mathbf{K}_m\nabla p\cdot\mathbf{n}_e\}[\xi]ds + \sum_{e\in\Gamma_0}\frac{\sigma_e}{|e|^\beta}\int_e[p][\xi]ds+\sum_{e\in\Gamma_0}\int_e\{\mathbf{K}_m\nabla\xi\cdot\mathbf{n}_e\}[p]ds, \tag{2.20}$$

$$a_l(p,\xi)=\int_l \epsilon k_f\frac{\partial p}{\partial\nu}\frac{\partial\xi}{\partial\nu}ds+\sum_{(x^*,y^*)\in X_f}\left(\epsilon k_f\left\{\frac{\partial p}{\partial\nu}\right\}\frac{\boldsymbol{\nu}\cdot\mathbf{n}_e}{|\boldsymbol{\nu}\cdot\mathbf{n}_e|}[\xi]+\epsilon k_f\left\{\frac{\partial\xi}{\partial\nu}\right\}\frac{\boldsymbol{\nu}\cdot\mathbf{n}_e}{|\boldsymbol{\nu}\cdot\mathbf{n}_e|}[p]+\frac{\alpha_e}{|e|^\gamma}[p][\xi]\right)\Big|_{(x^*,y^*)}. \tag{2.21}$$

$a_D(p,\xi)$ and $F(\xi)$ can be found in (2.13) and (2.14), respectively.

The existence and uniqueness of the EG solution is similar to those of DG method (Sun and Wheeler, 2005b). The DoF of EG method is much smaller than that of DG method, especially for low-order approximations. For example, for Q^1 polynomials in a 2-dimensional rectangular mesh with N_xN_y elements, the DG scheme has $4N_xN_y$ DoF, while EG scheme only has $(N_x+1)(N_y+1)+N_xN_y-1$ DoF. Detailed information about DoF can be found in Sun and Liu (2009).

As a contrast, we introduce IPDG scheme. In fact, we just replace W_h^{k,C_0} by W_h^k in (2.19). In Section 4, we numerically simulate the pressure equation with the above two methods. Obviously, EG and IPDG schemes with (2.11) or (2.19) are both symmetric. To be more precise, we use symmetric interior penalty Galerkin (SIPG) method (Sun and Wheeler, 2005b) with different discrete spaces.

2.4. IPDG method for the transport equation

After obtaining the pressure p from (2.19) by EG or IPDG method, we can calculate the velocity $\mathbf{u}$ as follows:

$$\mathbf{u}=-\mathbf{K}\nabla p,\quad x\in K\in\Omega_h, \tag{2.22}$$

$$\mathbf{u}\cdot\mathbf{n}=-\{\mathbf{K}\nabla p\cdot\mathbf{n}\}+\frac{\sigma_e}{|e|^\beta}(p|_{K_i}-p|_{K_j})+\frac{\alpha_e}{|e|^\gamma}\delta(\cdot)\mathbf{1}(\cdot)(p|_{K_i}-p|_{K_j})|\boldsymbol{\nu}\cdot\mathbf{n}|, \quad x\in e=\partial\overline{K_i}\cap\partial\overline{K_j},\ \textit{and}\ \mathbf{n}\ \textit{exterior to}\ K_i, \tag{2.23}$$

$$\mathbf{u}\cdot\mathbf{n}=p_N,\quad x\in\Gamma_N, \tag{2.24}$$

$$\mathbf{u}\cdot\mathbf{n}=-\mathbf{K}\nabla p\cdot\mathbf{n}+\frac{\sigma_e}{|e|^\beta}(p-p_D),\quad x\in\Gamma_D. \tag{2.25}$$

We note that $\mathbf{u}$ is defined at interior point in each element, while only the normal component of velocity $\mathbf{u}\cdot\mathbf{n}$ is defined on element interfaces and domain boundaries. The above velocity will be used in the transport equation.

Now we state the following theorem for the local mass conservation of the scheme.

Theorem 2.1. *Numerical scheme (2.19)–(2.25) defined above is locally conservative.*

Proof. Numerical solution $\mathbf{u}$ is locally conservative if

$$\int_{\partial K}\mathbf{u}\cdot\mathbf{n}_{\partial K}ds=\int_K qds. \tag{2.26}$$

In scheme (2.11), we take the test function $\xi=1\in W_h^{k,C_0}$ or W_h^k in each element K, then we will obtain (2.26). The proof of the theorem is complete. □

For the transport equation, we can employ IPDG method to obtain the numerical solution of concentration by seeking $r\in W_h^k$ such that for any $\zeta\in W_h^k$

$$(r_t,\zeta)=\mathcal{L}_c(\mathbf{u},c,\zeta)+\mathcal{L}_d(\mathbf{u},c,\zeta)+\mathcal{L}_s(\check{c},\zeta)+\mathcal{L}_B(\mathbf{u},c,\zeta), \tag{2.27}$$

where

$$\mathcal{L}_c(\mathbf{u},c,\zeta)=(\mathbf{u}c,\nabla\zeta)+\sum_{e\in\Gamma_0}\int_e\widehat{\mathbf{u}c}\cdot\mathbf{n}_e[\zeta]ds, \tag{2.28}$$

$$\mathcal{L}_d(\mathbf{u},c,\zeta)=-(\mathbf{D}(\mathbf{u})\nabla c,\nabla\zeta) -\sum_{e\in\Gamma_0}\int_e\left(\{\mathbf{D}(\mathbf{u})\nabla c\cdot\mathbf{n}_e\}[\zeta]+\{\mathbf{D}(u)\nabla\zeta\cdot\mathbf{n}_e\}[c]+\frac{\tilde{\alpha}}{|e|^\beta}[c][\zeta]\right)ds, \tag{2.29}$$

$$\mathcal{L}_s(\check{c},\zeta)=(\check{c}q,\zeta), \tag{2.30}$$

$$\mathcal{L}_B(\mathbf{u},c,\zeta)=-\sum_{e\in\Gamma_{in}}\int_e c_{in}(\mathbf{u}\cdot\mathbf{n}_{e,in})\zeta ds-\sum_{e\in\Gamma_{out}}\int_e c(\mathbf{u}\cdot\mathbf{n}_{e,out})\zeta ds-\sum_{e\in\Gamma_N}\int_e cp_N\zeta ds. \tag{2.31}$$

Here $\tilde{\alpha}$ and β is a positive constant to be chosen by the bound-preserving technique, $\mathbf{n}_{e,in}$, $\mathbf{n}_{e,out}$ are the unit outer normal vectors of $e\in\Gamma_{in}$ and $e\in\Gamma_{out}$, respectively,

$$c=P_k\left\{\frac{r}{\Phi}\right\},\quad \check{c}=\begin{cases}\tilde{c}, & q>0,\\ \frac{r}{\Phi}, & q<0,\end{cases} \tag{2.32}$$

and

$$\widehat{\mathbf{u}c}\cdot\mathbf{n}_e=(\mathbf{u}\cdot\mathbf{n}_e)\hat{c}=\begin{cases}(\mathbf{u}\cdot\mathbf{n}_e)c^-, & \mathbf{u}\cdot\mathbf{n}_e>0,\\ (\mathbf{u}\cdot\mathbf{n}_e)c^+, & \mathbf{u}\cdot\mathbf{n}_e<0.\end{cases} \tag{2.33}$$

Φ is L^2-projection of ϕ. P_k is the L^2-projection into W_h^k if $k\geq 2$ while $P_1(u)|_K$ is the interpolation of u at all vertices of cell K. These treatments are needed for bound-preserving techniques, which will be discussed in the next section. Moreover, like (2.11), IPDG scheme with (2.27) is also a symmetric form.

Now, we introduce the following definition that will be used in the bound-preserving technique (Guo and Yang, 2017).

Definition 2.1. We say two fluxes $\widehat{\mathbf{u}c}$, $\hat{\mathbf{u}}$ are consistent if $\widehat{\mathbf{u}c}=\hat{\mathbf{u}}$ by taking $c=1$ in Ω.

This definition was first introduced in Guo and Yang (2017) and was used to constructed the bound-preserving technique. From the definition, it is easy to obtain the following lemma.

Lemma 2.2. *The numerical flux pair* $(\mathbf{u}\cdot\mathbf{n}_e,\ \widehat{\mathbf{u}c}\cdot\mathbf{n}_e)$ *given in (2.23) and (2.33) are consistent.*

Next, we deal with $\mathbf{u}$ in the IPDG scheme for concentration c. Similar to the treatment of δ function in scheme of flow equation, we also need to use (2.17) and (2.18). More precisely,

$$(\mathbf{u}c,\nabla\zeta)\doteq-((\mathbf{K}_m\nabla p)c,\nabla\zeta)-\int_l\epsilon k_f c\frac{\partial p}{\partial\nu}\frac{\partial\zeta}{\partial\nu}ds, \tag{2.34}$$

$$\sum_{e\in\Gamma_0}\int_e \widehat{\mathbf{u}c}\cdot\mathbf{n}_e[\zeta]ds \doteq \sum_{e\in\Gamma_0}\int_e \hat{c}\left(-\{\mathbf{K}_m\nabla p\cdot\mathbf{n}_e\}-\frac{\sigma_e}{|e|^\beta}[p]\right)[\zeta]ds + \sum_{(x^*,y^*)\in X_f}\hat{c}\left(-\epsilon k_f\frac{\boldsymbol{\nu}\cdot\mathbf{n}_e}{|\boldsymbol{\nu}\cdot\mathbf{n}_e|}\left\{\frac{\partial p}{\partial\nu}\right\}-\frac{\alpha_e}{|e|^\gamma}[p]\right)[\zeta]\Big|_{(x^*,y^*)}. \tag{2.35}$$

For solving $\mathbf{u}$ used in $\mathbf{D}(\mathbf{u})$, we can simply apply the L^2 projection to $-\mathbf{K}\nabla p$, i.e. for any $\boldsymbol{\eta}\in\mathbf{W}_\mathbf{h}^\mathbf{k}:=W_h^k\times W_h^k$, $(\mathbf{u},\boldsymbol{\eta})=-(\mathbf{K}_m\nabla p,\boldsymbol{\eta})-\int_l \epsilon k_f\frac{\partial p}{\partial\nu}(\boldsymbol{\eta}\cdot\boldsymbol{\nu})ds$.

Based on (2.27), (2.34) and (2.35), we can obtain the final version of the IPDG scheme for (2.2) in fractured porous media: find $r\in W_h^k$ such that for any $\zeta\in W_h^k$

$$(r_t,\zeta)=\tilde{\mathcal{L}}_c(p,c,\zeta)+\tilde{\mathcal{L}}_d(\mathbf{u},c,\zeta)+\mathcal{L}_l(p,c,\zeta)+\mathcal{L}_s(\check{c},\zeta)+\tilde{\mathcal{L}}_B(p,c,\zeta), \tag{2.36}$$

where

$$\tilde{\mathcal{L}}_c(p,c,\zeta)=-((\mathbf{K}_m\nabla p)c,\nabla\zeta)+\sum_{e\in\Gamma_0}\int_e\hat{c}\left(-\{\mathbf{K}_m\nabla p\cdot\mathbf{n}_e\}-\frac{\sigma_e}{|e|^\beta}[p]\right)[\zeta]ds, \tag{2.37}$$

$$\tilde{\mathcal{L}}_d(\mathbf{u},c,\zeta)=-(\mathbf{D}(\mathbf{u})\nabla c,\nabla\zeta) -\sum_{e\in\Gamma_0}\int_e\left(\{\mathbf{D}(\mathbf{u})\nabla c\cdot\mathbf{n}_e\}[\zeta]+\{\mathbf{D}(\mathbf{u})\nabla\zeta\cdot\mathbf{n}_e\}[c]+\frac{\tilde{\alpha}}{|e|^\beta}[c][\zeta]\right)ds, \tag{2.38}$$

$$\mathcal{L}_l(p,c,\zeta)=-\int_l\epsilon k_f c\frac{\partial p}{\partial\nu}\frac{\partial\zeta}{\partial\nu}ds + \sum_{(x^*,y^*)\in X_f}\hat{c}\left(-\epsilon k_f\frac{\boldsymbol{\nu}\cdot\mathbf{n}_e}{|\boldsymbol{\nu}\cdot\mathbf{n}_e|}\left\{\frac{\partial p}{\partial\nu}\right\}-\frac{\alpha_e}{|e|^\gamma}[p]\right)[\zeta]\Big|_{(x^*,y^*)}, \tag{2.39}$$

$$\tilde{\mathcal{L}}_B(p,c,\zeta)=-\sum_{e\in\Gamma_N}\int_e cp_N\zeta ds-\sum_{e\in\Gamma_{in}}\int_e c_{in}\left(-\mathbf{K}_m\nabla p\cdot\mathbf{n}_{e,in}+\frac{\sigma_e}{|e|^\beta}(p-p_D)\right)\zeta ds - \sum_{e\in\Gamma_{out}}\int_e c\left(-\mathbf{K}_m\nabla p\cdot\mathbf{n}_{e,out}+\frac{\sigma_e}{|e|^\beta}(p-p_D)\right)\zeta ds, \tag{2.40}$$

and $\mathcal{L}_s(\check{c},\zeta)$ can be found in (2.30).

Remark 2.1. In above schemes (2.19) and (2.36), the shape of fracture l actually can be a curve, and the thickness ϵ and tangential permeability k_f of the fracture can be a scalar function defined along l. For the quadrature rule used for line integrals on l, one can refer to the remark 4.3 in Xu and Yang (2020). Note that if the fracture is straight and ϵ, k_f are constant, the midpoint rule is enough for Q^1 elements. In the case of fracture network, we just add all fracture terms together e.g. we can replace $-\int_l\epsilon k_f c\frac{\partial p}{\partial\nu}\frac{\partial\zeta}{\partial\nu}ds$ in (2.36) with $-\sum_{i=1}^{L}\int_{l_i}\epsilon_i k_{fi}c\frac{\partial p}{\partial\nu_i}\frac{\partial\zeta}{\partial\nu_i}ds$.

3. Bound-preserving technique

3.1. Second-order bound-preserving

In this section, we consider Euler forward time discretization and apply the bound-preserving technique to construct second-order physically relevant numerical approximations in $\mathbb{R}^2$. We first discuss the techniques for cells away from $\partial\Omega$, and the boundary cells can be analyzed following the same lines. We use o_{ij} for the numerical approximation o in K_{ij} and the cell average is $\bar{o}_{ij}$. Moreover, we use o^n to represent the solution o at time level n.

Before analyzing the bound-preserving schemes, we would like to demonstrate the following key points.

1. Approximate $r=\phi c$ directly instead of c. Due to the existence of ϕ in (2.2), we cannot extract the cell averages of c by simply taking the test function to be 1.
2. Take the L^2-projection of ϕ into W_h^k, denoted as Φ, which is the approximation of the porosity.
3. Construct a limiter to maintain the cell average $\bar{r}_{ij}$ and modify the numerical approximations of r_{ij} such that $0\le r_{ij}\le\Phi$, which further yields $c_{ij}=P_k(\frac{r_{ij}}{\Phi})\in[0,1]$, where P_k is the L^2-projection into W_h^k if $k\ge 2$ while $P_1c\,|_K$ is the interpolation of c at the four vertices of cell K.

In (2.27), we take $\zeta=1$ in K_{ij} (K_{ij} away from $\partial\Omega$) to obtain the equation satisfied by the cell average of r,

$$\bar{r}_{ij}^{n+1}=H^c(r,\mathbf{u},c)+H_x^d(r,\mathbf{u},c)+H_y^d(r,\mathbf{u},c)+H^s(r,\check{c},q), \tag{3.1}$$

where

$$H^c(r,\mathbf{u},c)=\frac{1}{3}\bar{r}_{ij}^n+\lambda\left(\int_{I_i}(\hat{c}\mathbf{u}\cdot\mathbf{n}_e)_{i,j-\frac12}-(\hat{c}\mathbf{u}\cdot\mathbf{n}_e)_{i,j+\frac12}dx + \int_{J_j}(\hat{c}\mathbf{u}\cdot\mathbf{n}_e)_{i-\frac12,j}-(\hat{c}\mathbf{u}\cdot\mathbf{n}_e)_{i+\frac12,j}dy\right), \tag{3.2}$$

$$H_x^d(r,\mathbf{u},c)=\frac{1}{6}\bar{r}_{ij}^n-\lambda\int_{J_j}\{D_{11}c_x+D_{12}c_y\}_{i-\frac12,j}-\{D_{11}c_x+D_{12}c_y\}_{i+\frac12,j} +\frac{\tilde{\alpha}}{|\Delta y|^\beta}[c]_{i-\frac12,j}-\frac{\tilde{\alpha}}{|\Delta y|^\beta}[c]_{i+\frac12,j}dy, \tag{3.3}$$

$$H_y^d(r,\mathbf{u},c)=\frac{1}{6}\bar{r}_{ij}^n-\lambda\int_{I_i}\{D_{21}c_x+D_{22}c_y\}_{i,j-\frac12}-\{D_{21}c_x+D_{22}c_y\}_{i,j+\frac12} +\frac{\tilde{\alpha}}{|\Delta x|^\beta}[c]_{i,j-\frac12}-\frac{\tilde{\alpha}}{|\Delta x|^\beta}[c]_{i,j+\frac12}dx, \tag{3.4}$$

$$H^s(r,\check{c},q)=\frac{1}{3}\bar{r}_{ij}^n+\Delta t\overline{\check{c}q}, \tag{3.5}$$

with $\lambda=\frac{\Delta t}{\Delta x\Delta y}$. We approximate the integrals above by using 2-point Gaussian quadratures. The Gaussian quadrature points on I_i and J_j are denoted by $\{x_i^1,x_i^2\}$ and $\{y_j^1,y_j^2\}$, respectively. The corresponding weights on the interval $[-\frac12,\frac12]$ are defined as w_1 and w_2. We will prove that if Δt is sufficiently small, then H^c, H_x^d, H_y^d, H^s are all positive, and the results are given in the following three lemmas. For simplicity of presentation, if the denominator in a fraction is zero, then the value of the fraction is defined as ∞.

Lemma 3.1. *Suppose $r^n>0(c^n>0)$, then $H^s(r,\check{c},q)>0$ under the condition*

$$\Delta t\le\frac{\Phi_m}{3q_M}, \tag{3.6}$$

where

$$\Phi_m=\min_{x,y}\Phi(x,y),\quad q_M=\max_{i,j,\beta,\gamma}\{-q(x_i^\beta,y_j^\gamma),0\}. \tag{3.7}$$

Lemma 3.2. *Suppose $r^n>0$ ($c^n>0$), then $H^c(r,\mathbf{u},c)>0$ under the condition*

$$\frac{\Delta t}{\Delta x}+\frac{\Delta t}{\Delta y}\le\frac{1}{6}B, \tag{3.8}$$

where

$$B=\min_{i,j,\beta}\left\{\frac{\Phi^-_{i+\frac12,j,\beta}}{|\mathbf{u}\cdot\mathbf{n}_e|_{i+\frac12,j,\beta}},\frac{\Phi^+_{i-\frac12,j,\beta}}{|\mathbf{u}\cdot\mathbf{n}_e|_{i-\frac12,j,\beta}},\frac{\Phi^-_{i,j+\frac12,\beta}}{|\mathbf{u}\cdot\mathbf{n}_e|_{i,j+\frac12,\beta}},\frac{\Phi^+_{i,j-\frac12,\beta}}{|\mathbf{u}\cdot\mathbf{n}_e|_{i,j-\frac12,\beta}}\right\}. \tag{3.9}$$

Lemma 3.3. *Suppose $r^n > 0 (c^n > 0)$, then $H_x^d(r, \mathbf{u}, c) > 0$ under the conditions*

$$\tilde{\alpha} \geq \frac{|\Delta y|^\beta}{2\Delta x} D_{11}^M + \sqrt{3}|\Delta y|^{\beta-1} D_{12}^M, \tag{3.10}$$

$$D_{11}^M \Lambda_1 + 2\left(\frac{\tilde{\alpha}}{|\Delta y|^{\beta-1}} + D_{12}^M\right)\lambda \leq \frac{1}{12}\Phi_m, \tag{3.11}$$

where

$$D_{11}^M = \max_{(x,y)\in\Omega} D_{11}(\mathbf{u})(x,y),\ D_{12}^M = \max_{(x,y)\in\Omega} |D_{12}(\mathbf{u})(x,y)|,\ \Lambda_1 = \frac{\Delta t}{\Delta x^2}. \tag{3.12}$$

Similarly, we have $H_y^d(r, \mathbf{u}, c) > 0$ if

$$\tilde{\alpha} \geq \frac{|\Delta x|^\beta}{2\Delta y} D_{22}^M + \sqrt{3}|\Delta x|^{\beta-1} D_{21}^M, \tag{3.13}$$

$$D_{22}^M \Lambda_2 + 2\left(\frac{\tilde{\alpha}}{|\Delta x|^{\beta-1}} + D_{21}^M\right)\lambda \leq \frac{1}{12}\Phi_m, \tag{3.14}$$

where

$$D_{22}^M = \max_{(x,y)\in\Omega} D_{22}(\mathbf{u})(x,y),\ D_{21}^M = \max_{(x,y)\in\Omega} |D_{21}(\mathbf{u})(x,y)|,\ \Lambda_2 = \frac{\Delta t}{\Delta y^2}. \tag{3.15}$$

We can find the proofs of Lemma 3.1 and Lemma 3.2 in Appendix B and Appendix C, respectively. For the diffusion terms $H_x^d((r, \mathbf{u}, c))$ and $H_y^d((r, \mathbf{u}, c))$, we can follow the same analysis in Guo and Yang (2017) with some minor changes. Therefore we skip the proof of Lemma 3.3. Next, base on the above three lemmas, we can state the following theorem.

Theorem 3.1. *Suppose $r^n > 0$ $(c^n > 0)$, and the parameters $\tilde{\alpha}$ satisfy (3.10), (3.11), (3.13) and (3.14). Then $\bar{r}_{ij}^{n+1} > 0$ under the conditions (3.6) and (3.8).*

Now, for these cells away from $\partial\Omega$, we have $\bar{r}_{ij}^{n+1} > 0$. To obtain $\bar{r}_{ij}^{n+1} \leq \bar{\Phi}$, we only need to prove $\bar{r}_{2ij}^{n+1} > 0$. Firstly, substituting (2.22)-(2.25) into (2.11) yields the following equation:

$$\begin{aligned} &-(\mathbf{u}, \nabla\xi) - \textstyle\sum_{e\in\Gamma_0} \int_e \mathbf{u}\cdot\mathbf{n}_e[\xi]ds + \sum_{e\in\Gamma_D} \int_e \mathbf{u}\cdot\mathbf{n}_{e,D}\xi ds \\ &+ \textstyle\sum_{e\in\Gamma_0} \int_e \{\mathbf{K}\nabla\xi\cdot\mathbf{n}_e\}[p]ds - \sum_{e\in\Gamma_D} \int_e \mathbf{K}\nabla\xi\cdot\mathbf{n}_{e,D} p ds \\ = \ &(q, \xi) - \textstyle\sum_{e\in\Gamma_N} \int_e p_N\xi ds - \sum_{e\in\Gamma_D} \int_e \mathbf{K}\nabla\xi\cdot\mathbf{n}_{e,D} p_D ds. \end{aligned} \tag{3.16}$$

Next, let $\xi = 1$ in (3.16) and $\zeta = 1$ in (2.27), then subtract (2.27) from (3.16), and use Lemma 2.2 to obtain

$$\bar{r}_{2ij}^{n+1} = H^c(r_2, \mathbf{u}, c_2) + H_x^d(r_2, \mathbf{u}, c_2) + H_y^d(r_2, \mathbf{u}, c_2) + H^s(r_2, \check{c}_2, q), \tag{3.17}$$

where $r_2 = \Phi - r$, $\check{c}_2 = 1 - \check{c}$. We can observe that the above equation is similar to (3.1). Therefore, following the same analysis above, we conclude that $\bar{r}_{2ij}^{n+1} > 0$ for these cells away from $\partial\Omega$, and the result is given below.

Theorem 3.2. *Suppose $0 \leq r_{ij}^n \leq \Phi$, and the conditions in Theorem 3.1 are satisfied, then $0 \leq \bar{r}_{ij}^{n+1} \leq \bar{\Phi}$.*

Next we study the cells near $\partial\Omega$. The boundary cells can be analyzed following the same lines with some minor changes except that the convection term is treated slightly differently because of the existence of the boundary. Without loss of generality, we take the last cell, denoted as K, as an example to illustrate this point. Let the left and lower boundaries of the last cell K are the interior interfaces, the upper boundary is the Neumann boundary for pressure equation, and the right boundary is the outflow boundary.

We take $\zeta = 1$ in K in (2.27) to obtain the equation satisfied by the cell average of r,

$$\bar{r}_K^{n+1} = H^{Bc}(r, \mathbf{u}, c) + H_x^{Bd}(r, \mathbf{u}, c) + H_y^{Bd}(r, \mathbf{u}, c) + H^s(r, \check{c}, q), \tag{3.18}$$

where

$$\begin{aligned} H^{Bc}(r, \mathbf{u}, c) = &\frac{1}{3}\bar{r}_{ij}^n + \lambda \int_{I_i} (\hat{c}\mathbf{u}\cdot\mathbf{n}_e)_{i,j-\frac{1}{2}} - (c^- p_N)_{i,j+\frac{1}{2}} dx \\ &+ \lambda \int_{J_j} (\hat{c}\mathbf{u}\cdot\mathbf{n}_e)_{i-\frac{1}{2},j} - (c^-\mathbf{u}\cdot\mathbf{n}_{e,out})_{i+\frac{1}{2},j} dy, \end{aligned} \tag{3.19}$$

$$H_x^{Bd}(r, \mathbf{u}, c) = \frac{1}{6}\bar{r}_{ij}^n - \lambda \int_{J_j} \{D_{11}c_x + D_{12}c_y\}_{i-\frac{1}{2},j} + \frac{\tilde{\alpha}}{|\Delta y|^\beta}[c]_{i-\frac{1}{2},j} dy, \tag{3.20}$$

$$H_y^{Bd}(r, \mathbf{u}, c) = \frac{1}{6}\bar{r}_{ij}^n - \lambda \int_{I_i} \{D_{21}c_x + D_{22}c_y\}_{i,j-\frac{1}{2}} + \frac{\tilde{\alpha}}{|\Delta x|^\beta}[c]_{i,j-\frac{1}{2}} dx, \tag{3.21}$$

with $i = N_x$, $j = N_y$.

The positivity of source term was given in Lemma 3.1 and the diffusion part can be analyzed following the same lines with some minor changes in Guo and Yang (2017). Hence we only focus on the convection part, and we have the following conclusion for $H^{Bc}(r, \mathbf{u}, c)$:

$$H^{Bc}(r, \mathbf{u}, c) > 0, \tag{3.22}$$

if

$$\frac{\Delta t}{\Delta x} + \frac{\Delta t}{\Delta y} \leq A, \tag{3.23}$$

where $A = \min_\beta \left\{ \frac{\Phi^-_{i+\frac{1}{2},j,\beta}}{6(\mathbf{u}\cdot\mathbf{n}_{e,out})_{i+\frac{1}{2},j,\beta}}, \frac{\Phi^-_{i,j+\frac{1}{2},\beta}}{6\max_\beta\{(p_N)_{i,j+\frac{1}{2},\beta}, 0\}}, \frac{\Phi^+_{i,j-\frac{1}{2},\beta}}{6\max\{(-\mathbf{u}\cdot\mathbf{n}_e)_{i,j-\frac{1}{2},\beta}, 0\}}, \frac{\Phi^+_{i-\frac{1}{2},j,\beta}}{6\max\{(-\mathbf{u}\cdot\mathbf{n}_e)_{i-\frac{1}{2},j,\beta}, 0\}} \right\}$.

We put the proof of (3.22) in Appendix D. Moreover, similar to the construction of (3.17), we can conclude that the cell average expression for r_2 is similar to the cell average for r. Therefore, $0 \leq \bar{r} \leq \bar{\Phi}$ for boundary cells.

Remark 3.1. The treatment of r_2 is different from that in Guo and Yang (2017) and Chuenjarern et al. (2019). In these two works, we subtract the scheme of the concentration equation from that of the pressure equation to obtain that of the second concentration. However, with the combination of EG and DG, it is impossible to subtract (3.16) and (2.27) due to the mismatch of the finite element spaces. However, what we want is not the full scheme, but the cell averages. Therefore, we took the test function to be 1 before we perform the subtraction.

3.2. Slope limiter

With Theorem 3.2, we can guarantee the numerical cell averages $\bar{r}$ to be physically relevant. However, the numerical approximation r may be negative or larger than Φ. Therefore, we need to apply a limiter to modify r. As discussed in Chuenjarern et al. (2019), the procedure is given in the following steps.

1. Define $\hat{S} = \{x \in K : r(x) \leq 0\}$. Take

$$\hat{r} = r + \theta\left(\frac{\bar{r}}{\bar{\Phi}}\Phi - r\right), \quad \theta = \max_{x\in\hat{S}} \left\{ \frac{-r(x)\bar{\Phi}}{\bar{r}\Phi(x) - r(x)\bar{\Phi}}, 0 \right\};$$

2. set $r_2 = \Phi - \hat{r}$, and repeat the above step for r_2;
3. Take $\tilde{r} = \Phi - \hat{r}_2$ as the new approximation.

Remark 3.2. After the above three steps, we have $0 \leq \tilde{r} \leq \Phi$. It is easy to check that the limiter does not change the numerical cell average, i.e. $\int_K \tilde{r}(x)dx = \int_K r(x)dx$. Moreover, it is proved that the limiter does not affect the accuracy. See Chuenjarern et al. (2019) for more information.

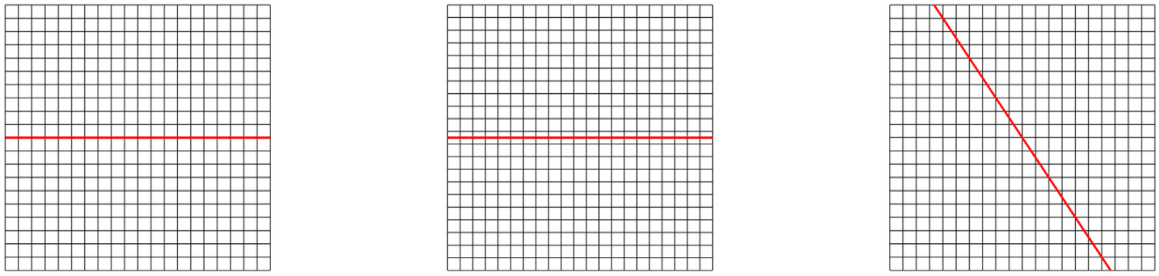

(a) θ=0, N_x=N_y=20 (b) θ=0, N_x=N_y=21 (c) θ=5.3, N_x=N_y=20

Fig. 2. Fracture and mesh settings with different θ of Example 4.1.

Table 1
Accuracy test for solving p using Q^1 polynomials of Example 4.1.

θ	$N_x \times N_y$	$\|\|err\|\|_{L^1(\Omega)}$	order	$\|\|err\|\|_{L^2(\Omega)}$	order	$\|\|err\|\|_{L^\infty(\Omega)}$	order
	20×20	1.199882e+00	–	3.369878e-01	–	3.609472e-01	–
$\theta = 0$	40×40	3.135942e-01	1.9359	8.908771e-02	1.9194	1.053578e-01	1.7765
	80×80	7.924337e-02	1.9845	2.250215e-02	1.9852	2.807924e-02	1.9077
	160×160	1.986708e-02	1.9959	5.636740e-03	1.9971	7.229529e-03	1.9575
	320×320	4.977799e-03	1.9968	1.410260e-03	1.9989	1.828045e-03	1.9836
	21×21	1.532164e+00	–	3.464954e-01	–	3.305671e-01	–
$\theta = 0$	41×41	5.298448e-01	1.5319	1.133726e-01	1.6118	1.002044e-01	1.7220
	81×81	2.003850e-01	1.4028	4.240577e-02	1.4187	2.732928e-02	1.8744
	161×161	8.417335e-02	1.2513	1.857249e-02	1.1911	1.007379e-02	1.4398
	321×321	4.118056e-02	1.0314	9.305575e-03	0.9970	4.245206e-03	1.2467
	20×20	1.388992e+00	–	4.224689e-01	–	6.260940e-01	–
$\theta = 5.3$	40×40	4.535562e-01	1.6147	1.197776e-01	1.8185	1.846778e-01	1.7614
	80×80	1.860685e-01	1.2854	4.185046e-02	1.5170	4.965249e-02	1.8951
	160×160	8.773946e-02	1.0845	1.964721e-02	1.0909	1.627395e-02	1.6093
	320×320	4.422695e-02	0.9883	9.875491e-03	0.9924	6.813483e-03	1.2561

Table 2
Accuracy test for solving p using Q^2 polynomials of Example 4.1.

θ	$N_x \times N_y$	$\|\|err\|\|_{L^1(\Omega)}$	order	$\|\|err\|\|_{L^2(\Omega)}$	order	$\|\|err\|\|_{L^\infty(\Omega)}$	order
	20×20	1.018221e-01	–	2.282509e-02	–	3.192690e-02	–
$\theta = 0$	40×40	1.326800e-02	2.9400	2.977359e-03	2.9385	4.220201e-03	2.9194
	80×80	1.669600e-03	2.9904	3.743863e-04	2.9914	5.325612e-04	2.9863
	160×160	2.089172e-04	2.9985	4.682947e-05	2.9990	6.667760e-05	2.9977
	320×320	2.611827e-05	2.9998	5.854090e-06	2.9999	8.335856e-06	2.9998
	21×21	1.320787e-01	–	3.143824e-02	–	2.425627e-02	–
$\theta = 0$	41×41	6.905574e-02	0.9356	1.678817e-02	0.9051	1.370998e-02	0.8231
	81×81	3.552099e-02	0.9591	8.606942e-03	0.9639	7.150747e-03	0.9391
	161×161	1.792659e-02	0.9866	4.318142e-03	0.9951	3.632414e-03	0.9772
	321×321	9.002522e-03	0.9937	2.164465e-03	0.9964	1.839774e-03	0.9814
	20×20	1.786417e-01	–	4.178467e-02	–	3.655140e-02	–
$\theta = 5.3$	40×40	8.446352e-02	1.0807	2.070221e-02	1.0132	2.086347e-02	0.8089
	80×80	4.326850e-02	0.9650	1.063492e-02	0.9610	1.151226e-02	0.8578
	160×160	2.266673e-02	0.9327	5.523742e-03	0.9451	6.144501e-03	0.9058
	320×320	1.153547e-02	0.9745	2.786098e-03	0.9874	3.170029e-03	0.9548

3.3. High-order time discretization

In this subsection, we introduce third-order strong stability preserving (SSP) time discretization to solve the ODE system $\mathbf{o}_t = \mathbf{L}(\mathbf{o})$, which is a convex combination of Euler forward time discretization. We consider the SSP Runge-Kutta method

$$\begin{aligned} \mathbf{o}^{(1)} &= \mathbf{o}^n + \Delta t \mathbf{L}(\mathbf{o}^n, t^n), \\ \mathbf{o}^{(2)} &= \tfrac{3}{4}\mathbf{o}^n + \tfrac{1}{4}\left(\mathbf{o}^{(1)} + \Delta t \mathbf{L}(\mathbf{o}^{(1)}, t^{n+1})\right), \\ \mathbf{o}^{n+1} &= \tfrac{1}{3}\mathbf{o}^n + \tfrac{2}{3}\left(\mathbf{o}^{(2)} + \Delta t \mathbf{L}(\mathbf{o}^{(2)}, t^n + \tfrac{\Delta t}{2})\right), \end{aligned} \tag{3.24}$$

and the multi-step method

$$\mathbf{o}^{n+1} = \frac{16}{27}(\mathbf{o}^n + 3\Delta t \mathbf{L}(\mathbf{o}^n, t^n)) + \frac{11}{27}\left(\mathbf{o}^{n-3} + \frac{12}{11}\Delta t \mathbf{L}(\mathbf{o}^{n-3}, t^{n-3})\right). \tag{3.25}$$

More details of these time discretizations can be found in Gottlieb et al. (2001, 2009); Shu (1988).

4. Numerical experiments

In this section, we provide numerical examples to illustrate the convergence and accuracy of RDFM based on the EG and IPDG methods on non-conforming meshes and effectiveness of the bound-preserving technique. We use the third-order SSP Runge-Kutta method (3.24). For the sake of simplicity, the flows in these tests are driven by boundary conditions instead of source term, i.e. $q = 0$.

In Example 4.1, we use Q^1 polynomials and Q^2 polynomials to construct the finite element space respectively and test the accuracy of EG method for solving RDFM. In Example 4.2, Q^1 polynomials are used. To test the effectiveness of the bound-preserving technique, we simulate the example with/without the bound-preserving limiter for incompressible miscible displacements in fractured porous media and compare the results. Example 4.3 is a realistic case in Flemisch et al. (2018), where Q^1

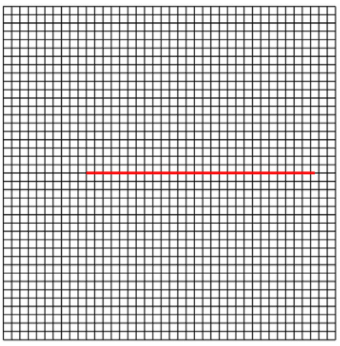

(a) Fracture and mesh settings

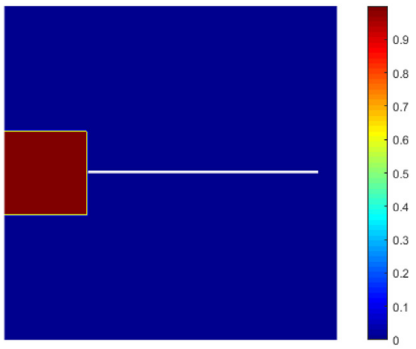

(b) Initial concentration

Fig. 3. Fracture setting and initial concentration of Example 4.2 on 40×40 mesh.

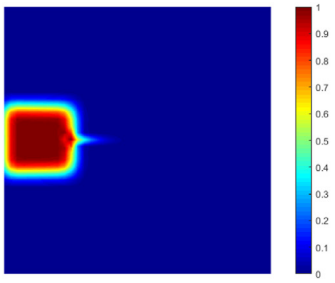

(a) T=0.1

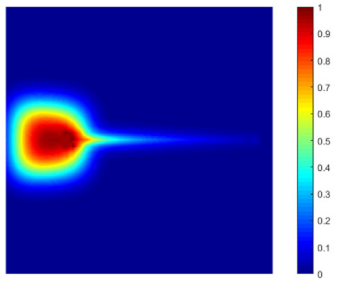

(b) T=0.5

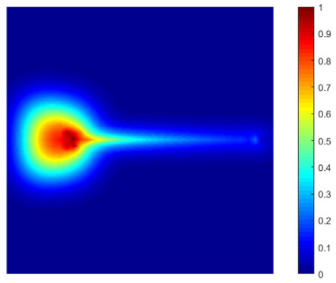

(c) T=0.9

Fig. 4. Concentration c with limiter of Example 4.2.

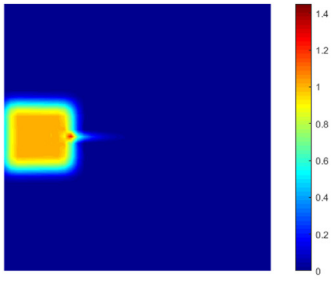

(a) T=0.1

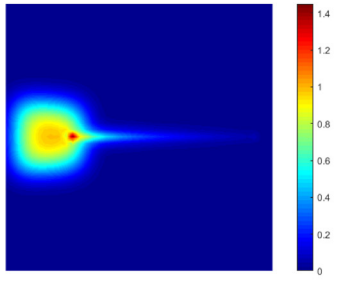

(b) T=0.5

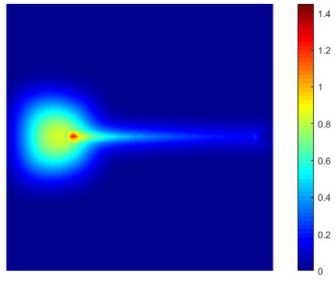

(c) T=0.9

Fig. 5. Concentration c without limiter of Example 4.2.

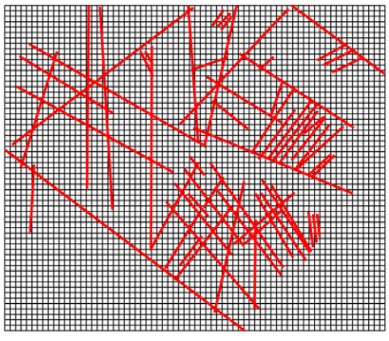

Fig. 6. Domain of Example 4.3 on 70×60 mesh.

polynomials are used to simulate contaminant propagation in fractured porous media.

Example 4.1. Accuracy test of EG method

In this example, we test the accuracy of EG method by solving the following problem:

$$-\nabla \cdot (\mathbf{K}\nabla p) = 0, \quad x \in \Omega = [-\pi, \pi] \times [-\pi, \pi],$$

where $\mathbf{K} = \mathbf{I} + 2\delta(-\sin(\theta)x + \cos(\theta)y)\begin{bmatrix} \cos^2(\theta) & \sin(\theta)\cos(\theta) \\ \sin(\theta)\cos(\theta) & \sin^2(\theta) \end{bmatrix}$, θ is an arbitrary fixed number.

The exact solution for any fixed θ is

$$p(x, y) = \sin(\cos(\theta)x + \sin(\theta)y)e^{|-\sin(\theta)x+\cos(\theta)y|},$$

and the corresponding Dirichlet boundary conditions are used. The product of thickness and permeability is $\epsilon k_f = 2$ and permeability of porous matrix is $k_m = 1$. By choosing different θ's, meshes and polynomial degrees k in the finite element space, we can test accuracy of EG method for DFM comprehensively.

We take three tests with different settings of θ's on rectangular meshes, in which $\theta = 5.3$ is randomly chosen to make the fracture in-

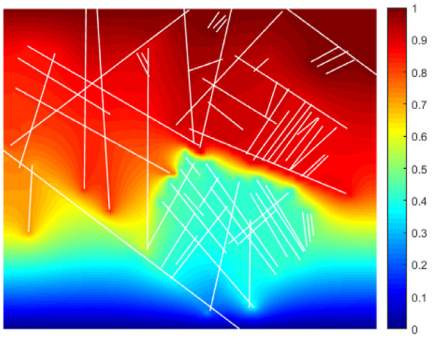

(a) Numerical results of p for case 1

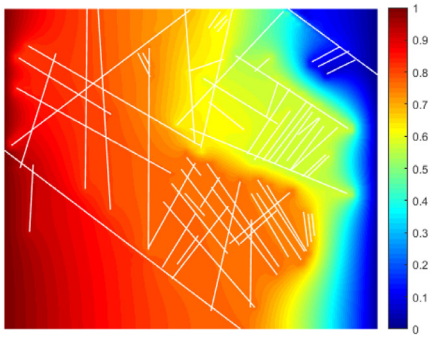

(b) Numerical results of p for case 2

Fig. 7. EG Numerical results of p in Example 4.3.

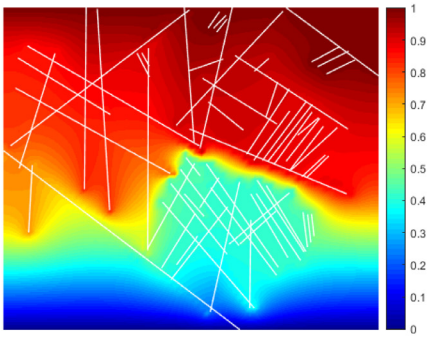

(a) Numerical results of p for case 1

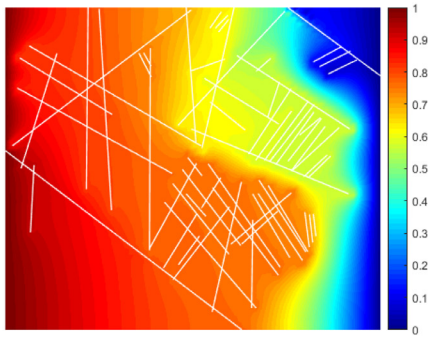

(b) Numerical results of p for case 2

Fig. 8. DG Numerical results of p in Example 4.3.

tersecting with gridcells non-conformingly. See Fig. 2 for illustration of settings of fracture and mesh. The numerical results are given in Table 1 and Table 2. From the tables, we can conclude that the EG method for the discrete fracture model is convergent. Moreover, we find the rates of convergence are optimal on conforming meshes and $O(h)$ on non-conforming meshes.

Example 4.2. Bound-preserving test

We use this example to show the significance of the bound-preserving technique in the simulation of miscible displacements in porous media. Let $\Omega = [0, 2\pi] \times [0, 2\pi]$. The initial concentrations c_0 is

$$c_0 = \begin{cases} 1, & 0 \le x \le \frac{\pi}{2}, \frac{3\pi}{4} \le y \le \frac{5\pi}{4}, \\ 0, & otherwise. \end{cases}$$

The left and right endpoints of the fracture are $(\frac{\pi}{2}, \pi)$, $(\frac{15\pi}{8}, \pi)$, respectively. See Fig. 3 for details of settings of fracture and concentration at $t = 0$ on 40×40 mesh. Other parameters are taken as

$$\phi = 1,\ \mathbf{K}_m = \mathbf{I},\ \epsilon k_f = 10^5,\ \mathbf{D} = 0.1\mathbf{I},\ c_{in} = 0.$$

Moreover, for pressure equation, the left, right boundaries are Dirichlet boundaries with pressure $p_{Dleft} = 2,\ p_{Dright} = 0$, while the bottom, top boundaries are Neumann boundaries with $p_N = 0$. The left boundary is the inflow boundary with $c_{in} = 0$. The right boundary is the outflow boundary.

We compute the concentration c at time $T = 0.1,\ 0.5,\ 0.9$s with $N_x = N_y = 40$ and $\Delta t = 0.001h^2$ ($h = \frac{2\pi}{40}$). The numerical results are shown in Fig. 4. From the figures we can see that the concentration c is between 0 and 1. To test the effectiveness of the bound-preserving technique, we simulate the example without the bound-preserving limiter, and the numerical results are shown in Fig. 5. We can conclude that the boundary preserving technique is effective.

Example 4.3. A Realistic Case

This example is a benchmark problem in Flemisch et al. (2018) modified from a real set of fractures from an interpreted outcrop in the Sotra island. The test case is a complex fracture network containing 63 fractures with different lengths and connectivity. For simplicity, the domain is uniformly shrunk to $\Omega = [0, 1.4] \times [0, 1.2]$ with permeability $K_m = 1$. The fractures on 70×60 mesh are shown in Fig. 6 with $\epsilon k_f = 10$. The detailed geometric data of fractures can be found in htt (0000) and Xu and Yang (2020), while we just scale down the geometry uniformly.

We simulate two cases. One case is that the contaminant propagates from top to bottom and the other case is that the contaminant propagates from left to right. Moreover, EG method and IPDG method introduced in Section 2 are used to solve pressure p respectively. The contour plots of numerical results for pressure equation are presented in Figs. 7 and 8.

Case 1: For pressure equation, the left, right boundaries are Neumann boundaries with $p_N = 0$, while the top, bottom boundaries are Dirichlet boundaries with $p_{Dtop} = 1,\ p_{Dbottom} = 0$, respectively. For concentration equation, the upper boundary is inflow boundary with $c_{in} = 1$, the lower boundary is outflow boundary with $c = c^+$, and the initial concentration is zero. The other parameters are taken as

$$\phi = 1,\ \mathbf{D} = 0.005|\mathbf{u}|\mathbf{I}.$$

We compute the concentration c at time $T = 0.01,\ 0.02,\ 0.03,\ 0.05,\ 0.08,\ 0.1$ with $N_x = 70,\ N_y = 60$ and $\Delta t = 0.0005h^2$ ($h = 0.02$). The numerical results are shown as Figs. 9 and 10, respectively.

Case 2: For pressure equation, the top, bottom boundaries are Neumann boundaries with $p_N = 0$, while the left, right boundaries are Dirichlet boundaries with $p_{Dleft} = 1,\ p_{Dright} = 0$. For concentration equation, the left boundary is inflow boundary with $c_{in} = 1$, the right

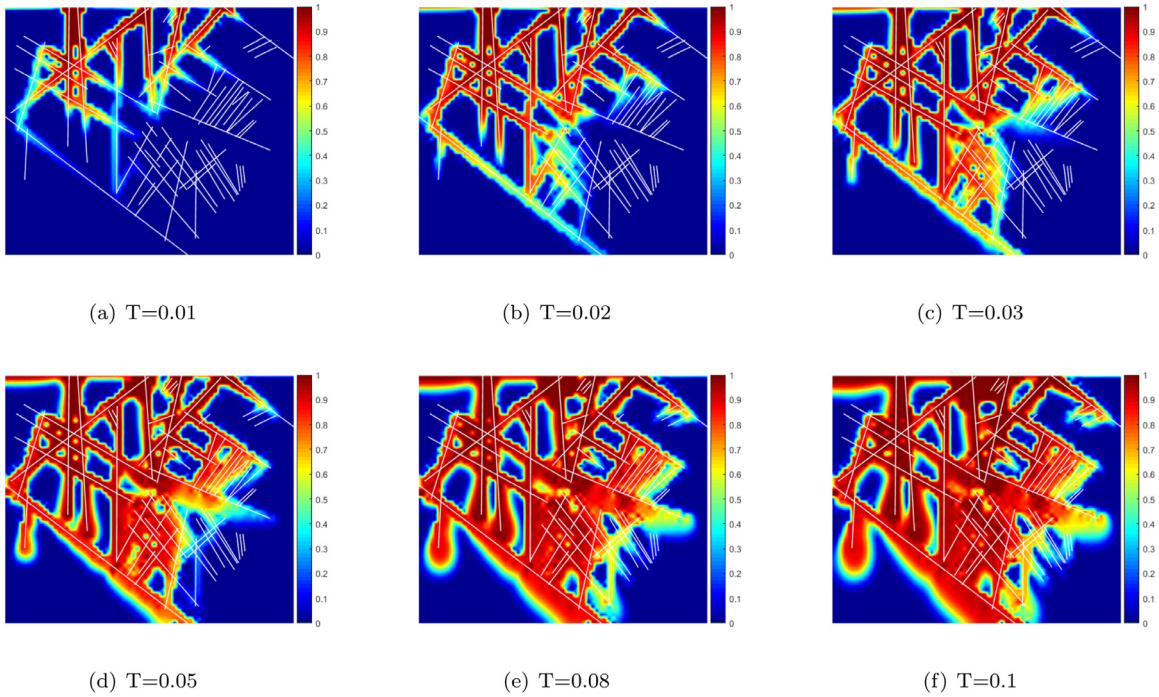

(a) T=0.01 (b) T=0.02 (c) T=0.03

(d) T=0.05 (e) T=0.08 (f) T=0.1

Fig. 9. Concentration c propagates from top to bottom at u^{EG} in Example 4.3.

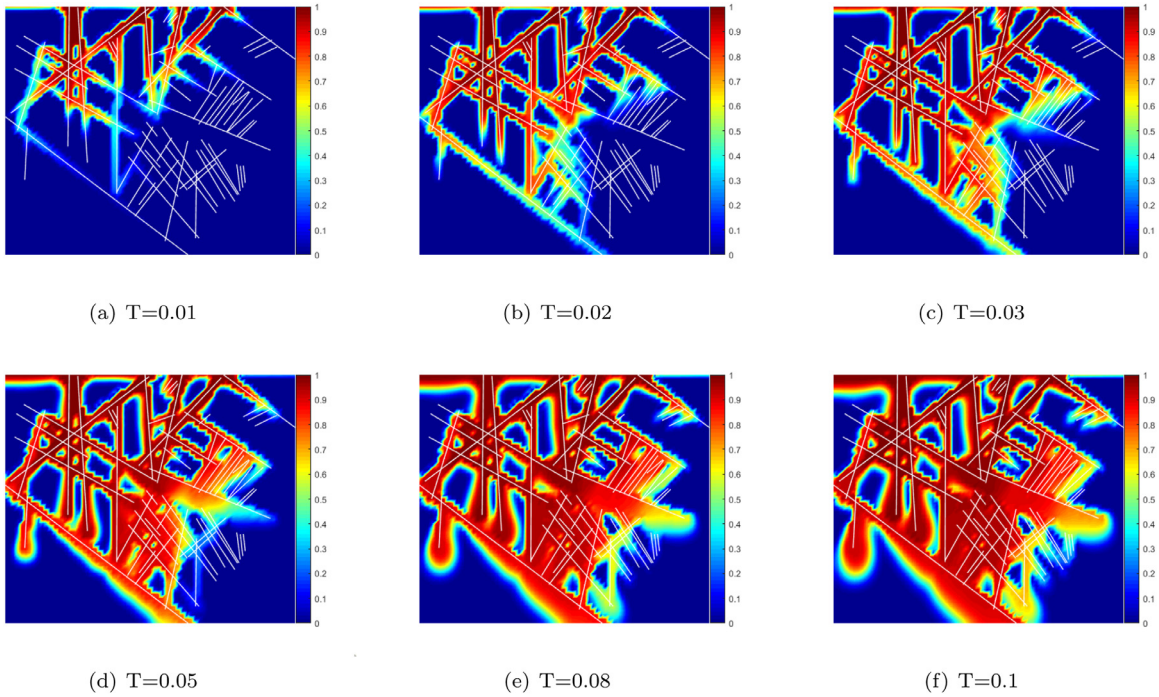

(a) T=0.01 (b) T=0.02 (c) T=0.03

(d) T=0.05 (e) T=0.08 (f) T=0.1

Fig. 10. Concentration c propagates from top to bottom at u^{DG} in Example 4.3.

boundary is outflow boundary with $c = c^-$, and the initial concentration is zero. The numerical results are shown as Figs. 11 and 12, respectively. Through the numerical simulation of above two cases, we can conclude that the numerical approximation of the concentration c is between 0 and 1, and the contaminants propagate along the fractures, which is in line with the relevant physical significance. In addition, the simulation results of EG method and IPDG method are almost the same, but the degree of freedom of the EG method is smaller than that of the IPDG method.

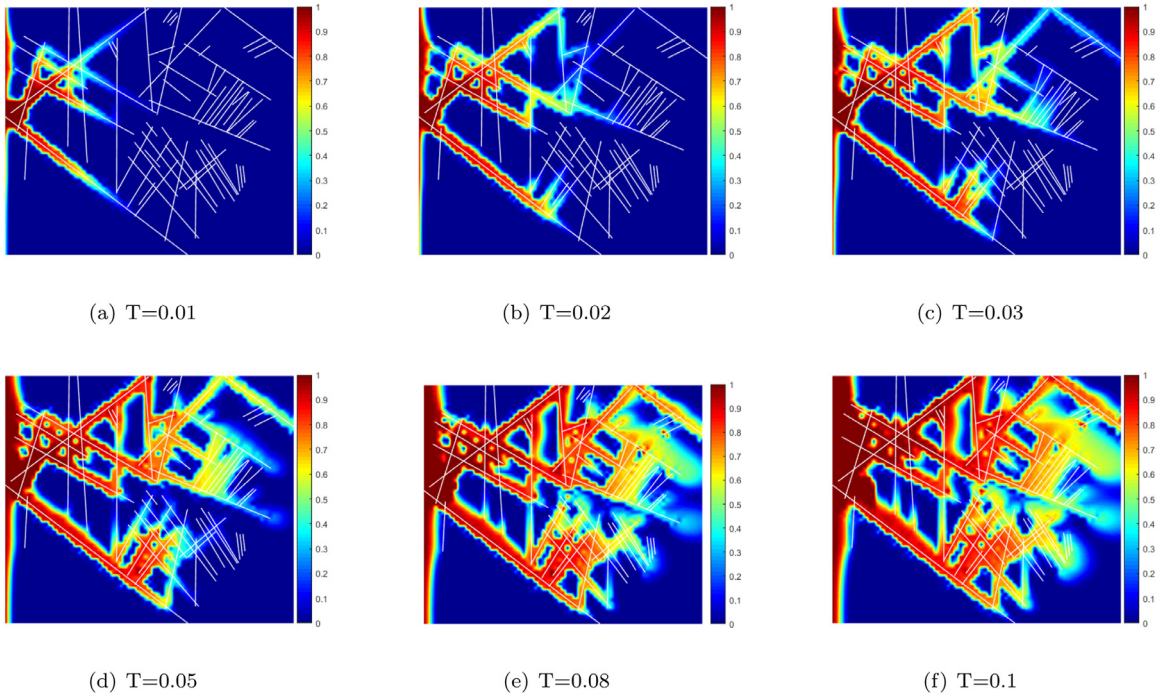

(a) T=0.01 (b) T=0.02 (c) T=0.03

(d) T=0.05 (e) T=0.08 (f) T=0.1

Fig. 11. Concentration c propagates from left to right at u^{EG} in Example 4.3.

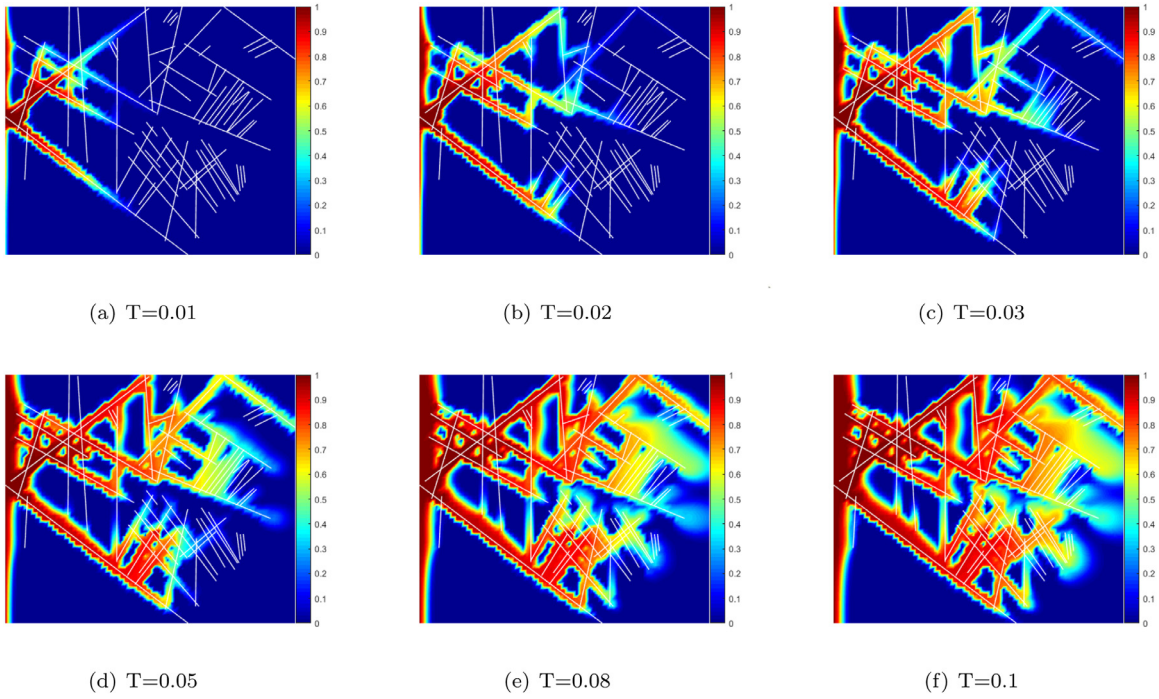

(a) T=0.01 (b) T=0.02 (c) T=0.03

(d) T=0.05 (e) T=0.08 (f) T=0.1

Fig. 12. Concentration c propagates from left to right at u^{DG} in Example 4.3.

5. Concluding remarks

In this paper, we combined the reinterpreted discrete fracture model with incompressible miscible displacements in porous media. We have derived the EG scheme and IPDG scheme for the flow equation and the IPDG scheme for the transport equation, and constructed conservative numerical fluxes, yielding local mass conservation. Moreover, the bound-preserving technique was applied by combining EG method and IPDG method. Theoretical analysis and numerical experiments showed effectiveness of the bound-preserving technique and good performance of RDFM based on the above two methods on non-conforming meshes.

In addition to the above, the explicit time method is used in this paper, which leads to small time step size. We can apply the implicit time methods, such as the implicit pressure explicit saturation (IMPES) method, and this is our future work. We will also discuss the multiphase flow, coupled hydro-mechanical problems and other similar problems in 3D in the future.

Declaration of Competing Interest

The authors declare that they have no known competing financial interests or personal relationships that could have appeared to influence the work reported in this paper.

Appendix A. Proof of Lemma 2.1

Proof. We parameterize the curve e locally around (x^*, y^*) as $x = x(t),\ y = y(t),\ t \in [t_0, t_1]$, and denote by $t^* \in [t_0, t_1]$ such that $x^* = x(t^*),\ y^* = y(t^*)$. By changing of variables and Taylor expansion, we have

$$
\begin{aligned}
&\int_e \delta(\cdot)\mathbf{1}(\cdot)g(x,y)ds \\
:&= \int_e \delta(-\sin(\theta)x + \cos(\theta)y - \eta_0)\mathbf{1}(\xi_1 \le \cos(\theta)x + \sin(\theta)y \le \xi_2)g(x,y)ds \\
&= \int_{t_0}^{t_1} \delta(-\sin(\theta)x(t) + \cos(\theta)y(t) - \eta_0)g(x(t),y(t))\sqrt{\dot{x}^2+\dot{y}^2}dt \\
&= \int_{t_0}^{t_1} \delta(-\sin(\theta)(x^* + \dot{x}(t^*)(t-t^*)) + \cos(\theta)(y^* + \dot{y}(t^*)(t-t^*)) - \eta_0)g(x(t),y(t))\sqrt{\dot{x}^2+\dot{y}^2}dt \\
&\quad \text{Change of variables } r = -\sin(\theta)(x^* + \dot{x}(t^*)(t-t^*)) + \cos(\theta)(y^* + \dot{y}(t^*)(t-t^*)) - \eta_0, \\
&= \int_{r(t_0)}^{r(t_1)} \delta(r)g(x(t(r)),y(t(r)))\sqrt{\dot{x}^2+\dot{y}^2}\frac{dr}{-\sin(\theta)\dot{x}(t^*) + \cos(\theta)\dot{y}(t^*)} \\
&\quad \text{Note that } r = 0 \Leftrightarrow t = t^*, \text{ by the property of } \delta \text{ function}, \\
&= g(x(t^*),y(t^*)) \cdot \left| \frac{\sqrt{\dot{x}^2(t^*)+\dot{y}^2(t^*)}}{-\sin(\theta)\dot{x}(t^*) + \cos(\theta)\dot{y}(t^*)} \right| \\
&= g(x^*,y^*) \cdot \frac{1}{\left| \cos(\theta)\frac{\dot{y}(t^*)}{\sqrt{\dot{x}^2(t^*)+\dot{y}^2(t^*)}} + \sin(\theta)\frac{-\dot{x}(t^*)}{\sqrt{\dot{x}^2(t^*)+\dot{y}^2(t^*)}} \right|} \\
&= g(x^*,y^*) \cdot \frac{1}{|\boldsymbol{\nu}\cdot\mathbf{n}_*|},
\end{aligned}
$$

where the last equality follows from $\boldsymbol{\nu} = (\cos(\theta), \sin(\theta))^T$ and $\mathbf{n}_* = \pm(\frac{\dot{y}(t^*)}{\sqrt{\dot{x}^2(t^*)+\dot{y}^2(t^*)}}, \frac{-\dot{x}(t^*)}{\sqrt{\dot{x}^2(t^*)+\dot{y}^2(t^*)}})^T$. Moreover, the linear Taylor expansion used in the third equality is accurate even for curved e, because δ is only supported at $\{0\}$. □

Appendix B. Proof of Lemma 3.1

Proof. The cell average of the source is approximated by the Gaussian quadrature:

$$
\begin{aligned}
H^s(r,\check{c},q) &= \tfrac{1}{3}\bar{r}_{ij}^n + \Delta t\overline{\check{c}q} \\
&= \tfrac{1}{3}\sum_{\beta=1}^2\sum_{\gamma=1}^2 w_\beta w_\gamma r_{ij}^n(x_i^\beta, y_j^\gamma) + \Delta t\sum_{\beta=1}^2\sum_{\gamma=1}^2 w_\beta w_\gamma(\check{c}q)(x_i^\beta, y_j^\gamma) \\
&:= \sum_{\beta=1}^2\sum_{\gamma=1}^2 w_\beta w_\gamma L_{\beta,\gamma},
\end{aligned}
$$

where

$$
L_{\beta,\gamma} := \frac{1}{3}r_{ij}^n(x_i^\beta, y_j^\gamma) + \Delta t(\check{c}q)(x_i^\beta, y_j^\gamma).
$$

Clearly, $L_{\beta,\gamma} > 0$ if $q(x_i^\beta, y_j^\gamma) \ge 0$. We only need to consider the case with $q(x_i^\beta, y_j^\gamma) < 0$. Without loss of generality, we assume $q(x_i^1, y_j^1) < 0$, then $\check{c}(x_i^1, y_j^1) = c(x_i^1, y_j^1)$. Notice that r_{ij}^n and c are both linear, then it is easy to check that

$$
\begin{aligned}
c(x_i^1, y_j^1) &= \mu_1^2 c_{i-\frac{1}{2},j-\frac{1}{2}} + \mu_1\mu_2 c_{i-\frac{1}{2},j+\frac{1}{2}} + \mu_1\mu_2 c_{i+\frac{1}{2},j-\frac{1}{2}} + \mu_2^2 c_{i+\frac{1}{2},j+\frac{1}{2}}, \\
r_{ij}^n(x_i^1, y_j^1) &= \mu_1^2 r_{i-\frac{1}{2},j-\frac{1}{2}} + \mu_1\mu_2 r_{i-\frac{1}{2},j+\frac{1}{2}} + \mu_1\mu_2 r_{i+\frac{1}{2},j-\frac{1}{2}} + \mu_2^2 r_{i+\frac{1}{2},j+\frac{1}{2}},
\end{aligned}
$$

with $\mu_1 = \frac{3+\sqrt{3}}{6}$ and $\mu_2 = \frac{3-\sqrt{3}}{6}$. Therefore,

$$
\begin{aligned}
L_{1,1} = \quad & \tfrac{1}{3}(\mu_1^2 r_{i-\frac{1}{2},j-\frac{1}{2}} + \mu_1\mu_2 r_{i-\frac{1}{2},j+\frac{1}{2}} + \mu_1\mu_2 r_{i+\frac{1}{2},j-\frac{1}{2}} + \mu_2^2 r_{i+\frac{1}{2},j+\frac{1}{2}}) \\
& + \Delta t q(x_i^1, y_j^1)(\mu_1^2 c_{i-\frac{1}{2},j-\frac{1}{2}} + \mu_1\mu_2 c_{i-\frac{1}{2},j+\frac{1}{2}} + \mu_1\mu_2 c_{i+\frac{1}{2},j-\frac{1}{2}} + \mu_2^2 c_{i+\frac{1}{2},j+\frac{1}{2}}) \\
= \quad & \mu_1^2 c_{i-\frac{1}{2},j-\frac{1}{2}}(\tfrac{1}{3}\Phi_{i-\frac{1}{2},j-\frac{1}{2}} + \Delta t q(x_i^1, y_j^1)) \\
& + \mu_1\mu_2 c_{i-\frac{1}{2},j+\frac{1}{2}}(\tfrac{1}{3}\Phi_{i-\frac{1}{2},j+\frac{1}{2}} + \Delta t q(x_i^1, y_j^1)) \\
& + \mu_1\mu_2 c_{i+\frac{1}{2},j-\frac{1}{2}}(\tfrac{1}{3}\Phi_{i+\frac{1}{2},j-\frac{1}{2}} + \Delta t q(x_i^1, y_j^1)) \\
& + \mu_2^2 c_{i+\frac{1}{2},j+\frac{1}{2}}(\tfrac{1}{3}\Phi_{i+\frac{1}{2},j+\frac{1}{2}} + \Delta t q(x_i^1, y_j^1)).
\end{aligned}
$$

Then we have $L_{1,1} > 0$ under the condition (3.6). □

Appendix C. Proof of Lemma 3.2

Proof. As the general treatment, we rewrite the cell average r_{ij}^n in the following form:

$$\bar{r}_{ij}^n = \sum_{\beta=1}^{2} \frac{w_\beta}{2}(r^+_{i-\frac{1}{2},j,\beta} + r^-_{i+\frac{1}{2},j,\beta}) = \sum_{\beta=1}^{2} \frac{w_\beta}{2}(r^+_{i,j-\frac{1}{2},\beta} + r^-_{i,j+\frac{1}{2},\beta}).$$

Denote $\lambda_1 = \frac{\Delta t}{\Delta x}$ and $\lambda_2 = \frac{\Delta t}{\Delta y}$, then

$$\begin{aligned} H^c(r,\mathbf{u},c) = \quad & \sum_{\beta=1}^{2} w_\beta\lambda_1\left[\frac{1}{6(\lambda_1+\lambda_2)}(r^+_{i-\frac{1}{2},j,\beta} + r^-_{i+\frac{1}{2},j,\beta}) + (\hat{c}\mathbf{u}\cdot\mathbf{n}_e)_{i-\frac{1}{2},j,\beta} - (\hat{c}\mathbf{u}\cdot\mathbf{n}_e)_{i+\frac{1}{2},j,\beta}\right] \\ & + \sum_{\beta=1}^{2} w_\beta\lambda_2\left[\frac{1}{6(\lambda_1+\lambda_2)}(r^+_{i,j-\frac{1}{2},\beta} + r^-_{i,j+\frac{1}{2},\beta}) + (\hat{c}\mathbf{u}\cdot\mathbf{n}_e)_{i,j-\frac{1}{2},\beta} - (\hat{c}\mathbf{u}\cdot\mathbf{n}_e)_{i,j+\frac{1}{2},\beta}\right]. \end{aligned}$$

Case 1: $\mathbf{u}\cdot\mathbf{n}_e$ is positive at all Gaussian points, then $\hat{c} = c^-$.

$$\begin{aligned} H^c(r,\mathbf{u},c) = \quad & \sum_{\beta=1}^{2} w_\beta\lambda_1\left[\frac{1}{6(\lambda_1+\lambda_2)}(r^+_{i-\frac{1}{2},j,\beta} + r^-_{i+\frac{1}{2},j,\beta}) + (c^-\mathbf{u}\cdot\mathbf{n}_e)_{i-\frac{1}{2},j,\beta} - (c^-\mathbf{u}\cdot\mathbf{n}_e)_{i+\frac{1}{2},j,\beta}\right] \\ & + \sum_{\beta=1}^{2} w_\beta\lambda_2\left[\frac{1}{6(\lambda_1+\lambda_2)}(r^+_{i,j-\frac{1}{2},\beta} + r^-_{i,j+\frac{1}{2},\beta}) + (c^-\mathbf{u}\cdot\mathbf{n}_e)_{i,j-\frac{1}{2},\beta} - (c^-\mathbf{u}\cdot\mathbf{n}_e)_{i,j+\frac{1}{2},\beta}\right] \\ = \quad & \sum_{\beta=1}^{2} w_\beta\lambda_1 c^+_{i-\frac{1}{2},j,\beta}\left(\frac{\Phi^+_{i-\frac{1}{2},j,\beta}}{6(\lambda_1+\lambda_2)}\right) + \sum_{\beta=1}^{2} w_\beta\lambda_1 c^-_{i+\frac{1}{2},j,\beta}\left(\frac{\Phi^-_{i+\frac{1}{2},j,\beta}}{6(\lambda_1+\lambda_2)} - (\mathbf{u}\cdot\mathbf{n}_e)_{i+\frac{1}{2},j,\beta}\right) \\ & + \sum_{\beta=1}^{2} w_\beta\lambda_1 c^-_{i-\frac{1}{2},j,\beta}(\mathbf{u}\cdot\mathbf{n}_e)_{i-\frac{1}{2},j,\beta} + \sum_{\beta=1}^{2} w_\beta\lambda_2 c^+_{i,j-\frac{1}{2},\beta}\left(\frac{\Phi^+_{i,j-\frac{1}{2},\beta}}{6(\lambda_1+\lambda_2)}\right) \\ & + \sum_{\beta=1}^{2} w_\beta\lambda_2 c^-_{i,j+\frac{1}{2},\beta}\left(\frac{\Phi^-_{i,j+\frac{1}{2},\beta}}{6(\lambda_1+\lambda_2)} - (\mathbf{u}\cdot\mathbf{n}_e)_{i,j+\frac{1}{2},\beta}\right) + \sum_{\beta=1}^{2} w_\beta\lambda_2 c^-_{i,j-\frac{1}{2},\beta}(\mathbf{u}\cdot\mathbf{n}_e)_{i,j-\frac{1}{2},\beta}. \end{aligned}$$

Then, $H^c(r,\mathbf{u},c) > 0$ if $(\lambda_1+\lambda_2)$ satisfy condition (3.8).

Case 2: $\mathbf{u}\cdot\mathbf{n}_e$ is negative at all Gaussian points, then $\hat{c} = c^+$.

$$\begin{aligned} H^c(r,\mathbf{u},c) = \quad & \sum_{\beta=1}^{2} w_\beta\lambda_1\left[\frac{1}{6(\lambda_1+\lambda_2)}(r^+_{i-\frac{1}{2},j,\beta} + r^-_{i+\frac{1}{2},j,\beta}) + (c^+\mathbf{u}\cdot\mathbf{n}_e)_{i-\frac{1}{2},j,\beta} - (c^+\mathbf{u}\cdot\mathbf{n}_e)_{i+\frac{1}{2},j,\beta}\right] \\ & + \sum_{\beta=1}^{2} w_\beta\lambda_2\left[\frac{1}{6(\lambda_1+\lambda_2)}(r^+_{i,j-\frac{1}{2},\beta} + r^-_{i,j+\frac{1}{2},\beta}) + (c^+\mathbf{u}\cdot\mathbf{n}_e)_{i,j-\frac{1}{2},\beta} - (c^+\mathbf{u}\cdot\mathbf{n}_e)_{i,j+\frac{1}{2},\beta}\right] \\ = \quad & \sum_{\beta=1}^{2} w_\beta\lambda_1 c^+_{i-\frac{1}{2},j,\beta}\left(\frac{\Phi^+_{i-\frac{1}{2},j,\beta}}{6(\lambda_1+\lambda_2)} + (\mathbf{u}\cdot\mathbf{n}_e)_{i-\frac{1}{2},j,\beta}\right) + \sum_{\beta=1}^{2} w_\beta\lambda_1 c^-_{i+\frac{1}{2},j,\beta}\left(\frac{\Phi^-_{i+\frac{1}{2},j,\beta}}{6(\lambda_1+\lambda_2)}\right) \\ & + \sum_{\beta=1}^{2} w_\beta\lambda_1 c^+_{i+\frac{1}{2},j,\beta}(-\mathbf{u}\cdot\mathbf{n}_e)_{i+\frac{1}{2},j,\beta} + \sum_{\beta=1}^{2} w_\beta\lambda_2 c^+_{i,j-\frac{1}{2},\beta}\left(\frac{\Phi^+_{i,j-\frac{1}{2},\beta}}{6(\lambda_1+\lambda_2)} + (\mathbf{u}\cdot\mathbf{n}_e)_{i,j-\frac{1}{2},\beta}\right) \\ & + \sum_{\beta=1}^{2} w_\beta\lambda_2 c^-_{i,j+\frac{1}{2},\beta}\left(\frac{\Phi^-_{i,j+\frac{1}{2},\beta}}{6(\lambda_1+\lambda_2)}\right) + \sum_{\beta=1}^{2} w_\beta\lambda_2 c^+_{i,j+\frac{1}{2},\beta}(-\mathbf{u}\cdot\mathbf{n}_e)_{i,j+\frac{1}{2},\beta}. \end{aligned}$$

Then, $H^c(r,\mathbf{u},c) > 0$ if $(\lambda_1+\lambda_2)$ satisfy condition (3.8).

Case 3: $\mathbf{u}\cdot\mathbf{n}_e$ can be positive or negative at Gaussian points. In fact, this case is a combination of *Case 1* and *Case 2*. Therefore, $H^c(r,\mathbf{u},c) > 0$ if condition (3.8) is true. □

Appendix D. Proof of (3.22)

Proof. We can write (3.19) as

$$\begin{aligned} H^{Bc}(r,\mathbf{u},c) = \quad & \sum_{\beta=1}^{2} w_\beta\left(\frac{\lambda_1}{6(\lambda_1+\lambda_2)}\left(r^+_{i-\frac{1}{2},j,\beta} + r^-_{i+\frac{1}{2},j,\beta}\right) + \frac{\lambda_2}{6(\lambda_1+\lambda_2)}\left(r^+_{i,j-\frac{1}{2},\beta} + r^-_{i,j+\frac{1}{2},\beta}\right)\right) \\ & + \sum_{\beta=1}^{2} w_\beta\lambda_1\left((\hat{c}\mathbf{u}\cdot\mathbf{n}_e)_{i-\frac{1}{2},j,\beta} - (c^-\mathbf{u}\cdot\mathbf{n}_{e,out})_{i+\frac{1}{2},j,\beta}\right) \\ & + \sum_{\beta=1}^{2} w_\beta\lambda_2\left((\hat{c}\mathbf{u}\cdot\mathbf{n}_e)_{i,j-\frac{1}{2},\beta} - (c^-p_N)_{i,j+\frac{1}{2},\beta}\right), \end{aligned}$$

where $\lambda_1 = \frac{\Delta t}{\Delta x}$ and $\lambda_2 = \frac{\Delta t}{\Delta y}$.

Case 1: $\mathbf{u}\cdot\mathbf{n}_e$ is positive at all Gaussian points, then $\hat{c} = c^-$.

$$\begin{aligned} H^{Bc}(r,\mathbf{u},c) = \quad & \sum_{\beta=1}^{2} w_\beta\lambda_1 c^+_{i-\frac{1}{2},j,\beta}\left(\frac{\Phi^+_{i-\frac{1}{2},j,\beta}}{6(\lambda_1+\lambda_2)}\right) + \sum_{\beta=1}^{2} w_\beta\lambda_1 c^-_{i+\frac{1}{2},j,\beta}\left(\frac{\Phi^-_{i+\frac{1}{2},j,\beta}}{6(\lambda_1+\lambda_2)} - (\mathbf{u}\cdot\mathbf{n}_{e,out})_{i+\frac{1}{2},j,\beta}\right) \\ & + \sum_{\beta=1}^{2} w_\beta\lambda_1 c^-_{i-\frac{1}{2},j,\beta}(\mathbf{u}\cdot\mathbf{n}_e)_{i-\frac{1}{2},j,\beta} + \sum_{\beta=1}^{2} w_\beta\lambda_2 c^+_{i,j-\frac{1}{2},\beta}\left(\frac{\Phi^+_{i,j-\frac{1}{2},\beta}}{6(\lambda_1+\lambda_2)}\right) \\ & + \sum_{\beta=1}^{2} w_\beta\lambda_2 c^-_{i,j+\frac{1}{2},\beta}\left(\frac{\Phi^-_{i,j+\frac{1}{2},\beta}}{6(\lambda_1+\lambda_2)} - (p_N)_{i,j+\frac{1}{2},\beta}\right) + \sum_{\beta=1}^{2} w_\beta\lambda_2 c^-_{i,j-\frac{1}{2},\beta}(\mathbf{u}\cdot\mathbf{n}_e)_{i,j-\frac{1}{2},\beta}. \end{aligned}$$

If

$$\lambda_1+\lambda_2 \le \min_\beta \left\{ \frac{\Phi^-_{i+\frac{1}{2},j,\beta}}{6(\mathbf{u}\cdot\mathbf{n}_{e,out})_{i+\frac{1}{2},j,\beta}}, \frac{\Phi^-_{i,j+\frac{1}{2},\beta}}{6\max_\beta\{(p_N)_{i,j+\frac{1}{2},\beta},0\}} \right\},$$

then $H^{Bc}>0$.

Case 2: $\mathbf{u}\cdot\mathbf{n}_e$ is negative at all Gaussian points, then $\hat{c}=c^+$.

$$\begin{aligned} H^{Bc}(r,\mathbf{u},c) = \quad & \sum_{\beta=1}^{2} w_\beta\lambda_1 c^+_{i-\frac{1}{2},j,\beta}\left(\frac{\Phi^+_{i-\frac{1}{2},j,\beta}}{6(\lambda_1+\lambda_2)}+(\mathbf{u}\cdot\mathbf{n}_e)_{i-\frac{1}{2},j,\beta}\right) \\ & +\sum_{\beta=1}^{2} w_\beta\lambda_1 c^-_{i+\frac{1}{2},j,\beta}\left(\frac{\Phi^-_{i+\frac{1}{2},j,\beta}}{6(\lambda_1+\lambda_2)}-(\mathbf{u}\cdot\mathbf{n}_{e,out})_{i+\frac{1}{2},j,\beta}\right) \\ & +\sum_{\beta=1}^{2} w_\beta\lambda_2 c^+_{i,j-\frac{1}{2},\beta}\left(\frac{\Phi^+_{i,j-\frac{1}{2},\beta}}{6(\lambda_1+\lambda_2)}+(\mathbf{u}\cdot\mathbf{n}_e)_{i,j-\frac{1}{2},\beta}\right) \\ & +\sum_{\beta=1}^{2} w_\beta\lambda_2 c^-_{i,j+\frac{1}{2},\beta}\left(\frac{\Phi^-_{i,j+\frac{1}{2},\beta}}{6(\lambda_1+\lambda_2)}-(p_N)_{i,j+\frac{1}{2},\beta}\right). \end{aligned}$$

If

$$\lambda_1+\lambda_2 \le A,$$

then $H^{Bc}>0$, where

$$A=\min_\beta\left\{ \frac{\Phi^-_{i+\frac{1}{2},j,\beta}}{6(\mathbf{u}\cdot\mathbf{n}_{e,out})_{i+\frac{1}{2},j,\beta}}, \frac{\Phi^-_{i,j+\frac{1}{2},\beta}}{6\max_\beta\{(p_N)_{i,j+\frac{1}{2},\beta},0\}}, \frac{\Phi^+_{i,j-\frac{1}{2},\beta}}{6\max\{(-\mathbf{u}\cdot\mathbf{n}_e)_{i,j-\frac{1}{2},\beta},0\}}, \frac{\Phi^+_{i-\frac{1}{2},j,\beta}}{6\max\{(-\mathbf{u}\cdot\mathbf{n}_e)_{i-\frac{1}{2},j,\beta},0\}} \right\}$$

Case 3: $\mathbf{u}\cdot\mathbf{n}_e$ is positive or negative at Gaussian points. Analogously, this case is a combination of *Case 1* and *Case 2*. Therefore, $H^{Bc}>0$ if $\lambda_1+\lambda_2\le A$.

To sum up, (3.22) is true under the condition (3.23). □

CRediT authorship contribution statement

Hui Guo: Conceptualization, Resources, Writing - review & editing, Supervision, Formal analysis. **Wenjing Feng:** Methodology, Software, Formal analysis, Writing - original draft. **Ziyao Xu:** Methodology, Software, Validation, Writing - review & editing. **Yang Yang:** Conceptualization, Methodology, Validation, Writing - review & editing, Visualization, Project administration, Funding acquisition.

References

Ahmed, R., Edwards, M.G., Lamine, S., Huisman, B.A., Pal, M., 2015. Control-volume distributed multi-point flux approximation coupled with a lower-dimensional fracture model. J. Comput. Phys. 284, 462–489. https://doi.org/10.1016/j.jcp.2014.12.047.

Alboin, C., Jaffré, J., Roberts, J.E., Wang, X., Serres, C., 2000. Domain decomposition for some transmission problems in flow in porous media. In: Numerical Treatment of Multiphase Flows in Porous Media. Springer, Berlin, Heidelberg, pp. 22–34. https://doi.org/10.1007/3-540-45467-5_2.

Angot, P., 2003. A model of fracture for elliptic problems with flux and solution jumps. C. R. Math. 337 (6), 425–430. https://doi.org/10.1016/S1631-073X(03)00300-5.

Angot, P., Boyer, F., Hubert, F., 2009. Asymptotic and numerical modelling of flows in fractured porous media. ESAIM 43 (2), 239–275. https://doi.org/10.1051/m2an/2008052.

Antonietti, P., Facciola, C., Russo, A., Verani, M., 2019. Discontinuous galerkin approximation of flows in fractured porous media on polytopic grids. SIAM J. Sci. Comput. (1) 41. https://doi.org/10.1137/17M1138194. A109-A138

Baca, R.G., Arnett, R.C., Langford, D.W., 1984. Modelling fluid flow in fractured-porous rock masses by finite-element techniques. Int. J. Numer. Methods Fluids 4 (4), 337–348. https://doi.org/10.1002/fld.1650040404.

Bartels, S., Jensen, M., Müller, R., 2009. Discontinuous Galerkin finite element convergence for incompressible miscible displacement problems of low regularity. SIAM J. Numer. Anal 47, 3720–3743. https://doi.org/10.1137/070712079.

Becker, R., Burman, E., Hansbo, P., Larson, M. G., 2003. A reduced p1-discontinuous Galerkin method. Chalmers Finite Element Center preprint 2003-13.

Burman, E., Hansbo, P., Larson, M.G., Larsson, K., 2019. Cut finite elements for convection in fractured domains. Comput. Fluids 179, 726–734. https://doi.org/10.1016/j.compfluid.2018.07.022.

Choo, J., Lee, S., 2018. Enriched Galerkin finite elements for coupled poromechanics with local mass conservation. Comput. Methods Appl. Mech. Eng. 341, 311–332. https://doi.org/10.1016/j.cma.2018.06.022.

Chou, S.-H., Li, Q., 1991. Mixed finite element methods for compressible miscible displacement in porous media. Math. Comp. 57, 507–527. https://doi.org/10.1090/S0025-5718-1991-1094942-7.

Chuenjarern, N., Xu, Z., Yang, Y., 2019. High-order bound-preserving discontinuous Galerkin methods for compressible miscible displacements in porous media on triangular meshes. J. Comput. Phys. 378, 110–128. https://doi.org/10.1016/j.jcp.2018.11.003.

Ţene, M., Bosma, S.B., Al Kobaisi, M.S., Hajibeygi, H., 2017. Projection-based embedded discrete fracture model (pEDFM). Adv. Water Resour. 105, 205–216. https://doi.org/10.1016/j.advwatres.2017.05.009.

Cui, M., 2008. Analysis of a semidiscrete discontinuous Galerkin scheme for compressible miscible displacement problem. J. Comput. Appl. Math. 214, 617–636. https://doi.org/10.1016/j.cam.2007.03.019.

Douglas jr, J., Ewing, R.E., Wheeler, M.F., 1983. The approximation of the pressure by a mixed method in the simulation of miscible displacement. RAIRO Anal. Numér. 17, 17–33. https://doi.org/10.1051/m2an/1983170100171.

Douglas Jr, J., Ewing, R.E., Wheeler, M.F., 1983. A time-discretization procedure for a mixed finite element approximation of miscible displacement in porous media. RAIRO Anal. Numér. 17, 249–265. https://doi.org/10.1051/m2an/1983170302491.

Douglas Jr., J., Roberts, J., 1983. Numerical methods for a model for compressible miscible displacement in porous media. Math. Comp. 41, 441–459. https://doi.org/10.1090/S0025-5718-1983-0717695-3.

Fang, W., Liu, C., Li, J., Jiang, H., Pu, J., Gu, H., Qin, X., 2018. A discrete modeling framework for reservoirs with complex fractured media: theory, validation and case studies. J. Pet. Sci. Eng. 170, 945–957. https://doi.org/10.1016/j.petrol.2017.11.050.

Flemisch, B., Berre, I., Boon, W., Fumagalli, A., Schwenck, N., Scotti, A., Stefansson, I., Tatomir, A., 2018. Benchmarks for single-phase flow in fractured porous media. Adv. Water Resour. 111, 239–258. https://doi.org/10.1016/j.advwatres.2017.10.036.

Flemisch, B., Fumagalli, A., Scotti, .A., 2016. A review of the XFEM-based approximation of flow in fractured porous media. In: Advances in Discretization Methods. Springer, Cham, pp. 47–76. https://doi.org/10.1007/978-3-319-41246-7_3.

Fumagalli, A., Scotti, A., 2014. An efficient XFEM approximation of darcy flows in arbitrarily fractured porous media. Oil Gas Sci. Technol. 69 (4), 555–564. https://doi.org/10.2516/ogst/2013192.

Gläser, D., Helmig, R., Flemisch, B., Class, H., 2017. A discrete fracture model for two-phase flow in fractured porous media. Adv. Water Resour. 110, 335–348. https://doi.org/10.1016/j.advwatres.2017.10.031.

Gottlieb, S., Ketcheson, D., Shu, C.W., 2009. High order strong stability preserving time discretizations. J. Sci. Comput. 38, 251–289. https://doi.org/10.1007/s10915-008-9239-z.

Gottlieb, S., Shu, C.-W., Tadmor, E., 2001. Strong stability-preserving high-order time discretization methods. SIAM Rev. 43, 89–112. https://doi.org/10.1137/S003614450036757X.

Guo, H., Liu, X., Yang, Y., 2020. High-order bound-preserving finite difference methods for miscible displacements in porous media. J. Comput. Phys. 406, 109219. https://doi.org/10.1016/j.jcp.2019.109219.

Guo, H., Yang, Y., 2017. Bound-preserving discontinuous Galerkin method for compressible miscible displacement in porous media. SIAM J. Sci. Comput. 39. https://doi.org/10.1137/16M1101313. A1969-A1990

Guo, H., Yu, F., Yang, Y., 2017. Local discontinuous Galerkin method for incompressible miscible displacement problem in porous media. J. Sci. Comput. 71, 615–633. https://doi.org/10.1007/s10915-016-0313-7.

Guo, H., Zhang, Q., 2015. Error analysis of the semi-discrete local discontinuous Galerkin method for compressible miscible displacement problem in porous media. Appl. Math. Comput. 259, 88–105. https://doi.org/10.1016/j.amc.2015.01.090.

Guo, H., Zhang, Q., Yang, Y., 2014. A combined mixed finite element method and local discontinuous Galerkin method for miscible displacement problem in porous media. Sci. China Math. 57, 2301–2320. https://doi.org/10.1007/s11425-014-4879-y.

https://git.iws.uni-stuttgart.de/benchmarks/fracture-flow.

Hansbo, A., Hansbo, P., 2002. An unfitted finite element method, based on Nitsche's method, for elliptic interface problems. Comput. Methods Appl. Mech. Eng. 191 (47–48), 5537–5552. https://doi.org/10.1016/S0045-7825(02)00524-8.

Hauck, M., Aizinger, V., Frank, F., et al., 2020. Enriched Galerkin method for the shallow-water equations. Int. J. Geomath. 11 (31). https://doi.org/10.1007/s13137-020-00167-7.

HosseiniMehr, M., Cusini, M., Vuik, C., Hajibeygi, H., 2018. Algebraic dynamic multilevel method for embedded discrete fracture model (f-ADM). J. Comput. Phys. 373, 324–345. https://doi.org/10.1016/j.jcp.2018.06.075.

Hoteit, H., Firoozabadi, A., 2005. Multicomponent fluid flow by discontinuous Galerkin and mixed methods in unfractured and fractured media. Water Resour. Res. 41 (11). https://doi.org/10.1029/2005WR004339.

Hoteit, H., Firoozabadi, A., 2006. Compositional modeling of discrete-fractured media without transfer functions by the discontinuous Galerkin and mixed methods. SPE J. 11 (03), 341–352. https://doi.org/10.2118/90277-PA.

Hoteit, H., Firoozabadi, A., 2008. Numerical modeling of two-phase flow in heterogeneous permeable media with different capillarity pressures. Adv. Water Resour. 31 (1), 56–73. https://doi.org/10.1016/j.advwatres.2007.06.006.

Huang, H., Long, T.A., Wan, J., Brown, W.P., 2011. On the use of enriched finite element method to model subsurface features in porous media flow problems. Comput. Geosci 15 (4), 721–736. https://doi.org/10.1007/s10596-011-9239-1.

Jiang, J., Younis, R.M., 2017. An improved projection-based embedded discrete fracture model (pEDFM) for multiphase flow in fractured reservoirs. Adv. Water Resour. 109, 267–289. https://doi.org/10.1016/j.advwatres.2017.09.017.

Kadeethum, T., Lee, S., Nick, H.M., 2020. Finite element solvers for biot's poroelasticity equations in porous media. Math. Geosci. 52, 977–1015. https://doi.org/10.1007/s11004-020-09893-y.
Kadeethum, T., Nick, H., Lee, S., Ballarin, F., 2020. Flow in porous media with low dimensional fractures by employing enriched Galerkin method. Adv. Water Resour. 142, 103620. https://doi.org/10.1016/j.advwatres.2020.103620.
Kadeethum, T., Nick, H.M., Lee, S., Ballarin, F., 2021. Enriched Galerkin discretization for modeling poroelasticity and permeability alteration in heterogeneous porous media. J. Comput. Phys. 427, 110030. https://doi.org/10.1016/j.jcp.2020.110030.
Karimi-Fard, M., Durlofsky, L.J., Aziz, K., 2003. An efficient discrete fracture model applicable for general purpose reservoir simulators. SPE Reservoir Simulation Symposium. Society of Petroleum Engineers. https://doi.org/10.2118/88812-PA.
Karimi-Fard, M., Firoozabadi, A., 2001. Numerical simulation of water injection in 2d fractured media using discrete-fracture model. In: SPE Annual Technical Conference and Exhibition, Society of Petroleum Engineers https://doi.org/10.2118/71615-MS.
Kim, J.G., Deo, M.D., 1999. Comparison of the performance of a discrete fracture multiphase model with those using conventional methods. SPE Reservoir Simulation Symposium, Society of Petroleum Engineers. https://doi.org/10.2118/51928-MS.
Kim, J.G., Deo, M.D., 2000. Finite element, discrete-fracture model for multiphase flow in porous media. AIChE J. 46 (6), 1120–1130. https://doi.org/10.1002/aic.690460604.
Köppel, M., Martin, V., Jaffré, J., Roberts, J.E., 2019. A lagrange multiplier method for a discrete fracture model for flow in porous media. Comput. Geosci. 23 (2), 239–253. https://doi.org/10.1007/s10596-018-9779-8.
Köppel, M., Martin, V., Roberts, J.E., 2019. A stabilized lagrange multiplier finite-element method for flow in porous media with fractures. GEM Int. J. Geomath. 10 (1), 7. https://doi.org/10.1007/s10596-018-9779-8.
Kumar, S., 2012. A mixed and discontinuous Galerkin finite volume element method for incompressible miscible displacement problems in porous media. Numer. Methods Partial Differ. Equ. 28, 1354–1381. https://doi.org/10.1002/num.20684.
Lee, S., Lee, Y., Wheeler, M., 2016. A locally conservative enriched Galerkin approximation and efficient solver for elliptic and parabolic problems. SIAM J. Sci. Comput. 38 (3). https://doi.org/10.1137/15M1041109. A1404-A1429
Lee, S., Mikelic, A., Wheeler, M., Wick, T., 2016. Phase-field modeling of proppant-filled fractures in a poroelastic medium. Comput. Methods Appl. Mech. Eng. 312, 509–541. https://doi.org/10.1016/j.cma.2016.02.008.
Lee, S., Mikelic, A., Wheeler, M., Wick, T., 2018. Phase-field modeling of two phase fluid filled fractures in a poroelastic medium. Multiscale Model. Simul. 16 (4), 1542–1580. https://doi.org/10.1137/17M1145239.
Lee, S., Wheeler, M., 2017. Adaptive enriched Galerkin methods for miscible displacement problems with entropy residual stabilization. J. Comput. Phys. 331, 19–37. https://doi.org/10.1016/j.jcp.2016.10.072.
Lee, S., Wheeler, M., 2018. Enriched Galerkin methods for two-phase flow in porous media with capillary pressure. J. Comput. Phys. 367, 65–86. https://doi.org/10.1016/j.jcp.2018.03.031.
Lee, S., Wheeler, M.F., 2020. Modeling interactions of natural and two-phase fluid-filled fracture propagation in porous media. Comput Geosci. https://doi.org/10.1007/s10596-020-09975-0.
Li, L., Lee, S.H., 2008. Efficient field-scale simulation of black oil in a naturally fractured reservoir through discrete fracture networks and homogenized media. SPE Reserv. Eval. Eng. 11 (04), 750–758. https://doi.org/10.2118/103901-PA.
Martin, V., Jaffré, J., Roberts, J.E., 2005. Modeling fractures and barriers as interfaces for flow in porous media. SIAM J. Sci. Comput. 26 (5), 1667–1691. https://doi.org/10.1137/S1064827503429363.
Moinfar, A., 2013. Development of an efficient embedded discrete fracture model for 3d compositional reservoir simulation in fractured reservoirs. 10.2118/154246-PA
Monteagudo, J.E., Firoozabadi, A., 2007. Control-volume model for simulation of water injection in fractured media: incorporating matrix heterogeneity and reservoir wettability effects. SPE J. 12 (03), 355–366. https://doi.org/10.2118/98108-PA.
Monteagudo, J.E.P., Firoozabadi, A., 2004. Control-volume method for numerical simulation of two-phase immiscible flow in two-and three-dimensional discrete-fractured media. Water Resour. Res. 40 (7). https://doi.org/10.1029/2003WR002996.
Monteagudo, J.E.P., Firoozabadi, A., 2007. Comparison of fully implicit and IMPES formulations for simulation of water injection in fractured and unfractured media. Int. J. Numer. Methods Eng. 69 (4), 698–728. https://doi.org/10.1002/nme.1783.
Moortgat, J., Amooie, M.A., Soltanian, M.R., 2016. Implicit finite volume and discontinuous Galerkin methods for multicomponent flow in unstructured 3d fractured porous media. Adv. Water Resour. 96, 389–404. https://doi.org/10.1016/j.advwatres.2016.08.007.
Moortgat, J., Firoozabadi, A., 2013. Higher-order compositional modeling of three-phase flow in 3d fractured porous media based on cross-flow equilibrium. J. Comput. Phys. 250, 425–445. https://doi.org/10.1016/j.jcp.2013.05.009.
Moortgat, J., Firoozabadi, A., 2013. Three-phase compositional modeling with capillarity in heterogeneous and fractured media. SPE J. 18 (06), 1–150. https://doi.org/10.2118/159777-MS.
Noorishad, J., Mehran, M., 1982. An upstream finite element method for solution of transient transport equation in fractured porous media. Water Resour. Res. 18 (3), 588–596. https://doi.org/10.1029/WR018i003p00588.
Reichenberger, V., Jakobs, H., Bastian, P., Helmig, R., 2006. A mixed-dimensional finite volume method for two-phase flow in fractured porous media. Adv. Water Resour. 29 (7), 1020–1036. https://doi.org/10.1016/j.advwatres.2005.09.001.
Rivière, B., 2008. Discontinuous Galerkin methods for solving elliptic and parabolic equations: theory and implementation. SIAM https://doi.org/10.1137/1.9780898717440.
Rupp, A., Lee, S., 2020. Continuous Galerkin and enriched galerkin methods with arbitrary order discontinuous trial functions for the elliptic and parabolic problems with jump conditions. J. Sci. Comput. 84, 9. https://doi.org/10.1007/s10915-020-01255-4.
Salimzadeh, S., Khalili, N., 2015. Fully coupled XFEM model for flow and deformation in fractured porous media with explicit fracture flow. Int. J. Geomech. 16 (4), 04015091. https://doi.org/10.1061/(ASCE)GM.1943-5622.0000623.
Sandve, T.H., Berre, I., Nordbotten, J.M., 2012. An efficient multi-point flux approximation method for discrete fracture-matrix simulations. J. Comput. Phys. 231 (9), 3784–3800. https://doi.org/10.1016/j.jcp.2012.01.023.
Schädle, P., Zulian, P., Vogler, D., Bhopalam, S.R., Nestola, M.G., Ebigbo, A., Krause, R., Saar, M.O., 2019. 3d non-conforming mesh model for flow in fractured porous media using lagrange multipliers. Comput. Geosci. 132, 42–55. https://doi.org/10.1016/j.cageo.2019.06.014.
Shu, C.W., 1988. Total-variation-diminishing time discretizations. SIAM J. Sci. Stat. Comput 9, 1073–1084. https://doi.org/10.1137/0909073.
Sun, S., Liu, J., 2009. A locally consertative finite element method based on piecewise constant enrichment of the continuous Galerkin method. SIAM J. Sci. Comput. 31, 2528–2548. https://doi.org/10.1137/080722953.
Sun, S., Rivière, B., Wheeler, M.F., 2002. A combined mixed finite element and discontinuous Galerkin method for miscible displacement problem in porous media. In: Chan, T. (Ed.), Recent Progress in Computational and Applied PDEs, Kluwer Academic Publishers. Plenum Press, Dordrecht, New York, pp. 323–351. https://doi.org/10.1007/978-1-4615-0113-8_23.
Sun, S., Wheeler, M.F., 2005. Discontinuous Galerkin methods for coupled flow and reactive transport problems. Appl. Numer. Math. 52, 273–298. https://doi.org/10.1016/j.apnum.2004.08.035.
Sun, S., Wheeler, M.F., 2005. Symmetric and nonsymmetric discontinuous Galerkin methods for reactive transport in porous media. SIAM J. Numer. Anal. 43, 195–219. https://doi.org/10.1137/S003614290241708X.
ter, L.H.O., Kvamsdal, T., Larson, M.G., 2019. A simple embedded discrete fracture-matrix model for a coupled flow and transport problem in porous media. Comput. Methods Appl. Mech. Eng. 343, 572–601. https://doi.org/10.1016/j.cma.2018.09.003.
Wheeler, M., Wick, T., Lee, S., 2020. IPACS: integrated phase-field advanced crack propagation simulator. an adaptive, parallel, physics-based-discretization phase-field framework for fracture propagation in porous media. Comput. Methods Appl. Mech.Eng. 367, 113124. https://doi.org/10.1016/j.cma.2020.113124.
Xu, J., Sun, B., Chen, B., 2019. A hybrid embedded discrete fracture model for simulating tight porous media with complex fracture systems. J. Pet. Sci. Eng. 174, 131–143. https://doi.org/10.1016/j.petrol.2018.10.094.
Xu, Z., Yang, Y., 2020. The hybrid dimensional representation of permeability tensor: a reinterpretation of the discrete fracture model and its extension on nonconforming meshes. J. Comput. Phys. 415, 109523. https://doi.org/10.1016/j.jcp.2020.109523.
Yan, X., Huang, Z., Yao, J., Li, Y., Fan, D., 2016. An efficient embedded discrete fracture model based on mimetic finite difference method. J. Pet. Sci. Eng. 145, 11–21. https://doi.org/10.1016/j.petrol.2016.03.013.
Yang, J., 2011. A posteriori error of a discontinuous Galerkin scheme for compressible miscible displacement problems with molecular diffusion and dispersion. Int. J. Numer. Methods Fluids 65, 781–797. https://doi.org/10.1002/fld.2208.
Yu, F., Guo, H., Chuenjarern, N., Yang, Y., 2017. Conservative local discontinuous Galerkin method for compressible miscible displacements in porous media. J. Sci. Comput. 73, 1249–1275. https://doi.org/10.1007/s10915-017-0571-z.
Zhang, R.H., Zhang, L.H., Luo, J.X., Yang, Z.D., Xu, M.Y., 2016. Numerical simulation of water flooding in natural fractured reservoirs based on control volume finite element method. J. Pet. Sci. Eng. 146, 1211–1225. https://doi.org/10.1016/j.petrol.2016.08.024.
Zhang, X., Shu, C.W., 2010. On maximum-principle-satisfying high order schemes for scalar conservation laws. J. Comput. Phys. 229, 3091–3120. https://doi.org/10.1016/j.jcp.2009.12.030.
Zidane, A., Firoozabadi, A., 2014. An efficient numerical model for multicomponent compressible flow in fractured porous media. Adv. Water Resour. 74, 127–147. https://doi.org/10.1016/j.advwatres.2014.08.010.